2011

Free Surface Confinement Effects on a Round Jet

Jiahao Tian
University of Windsor

FREE SURFACE CONFINEMENT EFFECTS ON A ROUND JET

by

Jiahao Tian

A Thesis
Submitted to the Faculty of Graduate Studies
through the Department of Mechanical, Automotive and Materials Engineering
in Partial Fulfillment of the Requirements for
the Degree of Master of Applied Science at the
University of Windsor

Windsor, Ontario, Canada

2010

FREE SURFACE CONFINEMENT EFFECTS ON A ROUND JET

by

Jiahao Tian

APPROVED BY:

_____

Dr. T. Bolisetti
Department of Civil and Environmental Engineering

_____

Dr. R. Barron
Department of Mechanical, Automotive, and Materials Engineering

_____

Dr. G. Rankin
Department of Mechanical, Automotive, and Materials Engineering

_____

Dr. R. Balachandar, Advisor
Department of Mechanical, Automotive, and Materials Engineering

_____

Dr. A. Fartaj, Chair of Defense
Department of Mechanical, Automotive, and Materials Engineering

16 December 2010

DECLARATION OF ORIGINALITY

I hereby certify that I am the sole author of this thesis and that no part of this thesis has been published or submitted for publication.

I certify that, to the best of my knowledge, my thesis does not infringe upon anyone's copyright nor violate any proprietary rights and that any ideas, techniques, quotations, or any other material from the work of other people included in my thesis, published or otherwise, are fully acknowledged in accordance with the standard referencing practices. Furthermore, to the extent that I have included copyrighted material that surpasses the bounds of fair dealing within the meaning of the Canada Copyright Act, I certify that I have obtained a written permission from the copyright owner(s) to include such material(s) in my thesis and have included copies of such copyright clearances to my appendix.

I declare that this is a true copy of my thesis, including any final revisions, as approved by my thesis committee and the Graduate Studies office, and that this thesis has not been submitted for a higher degree to any other University or Institution.

ABSTRACT

In this study, the characteristics of a round turbulent jet in the vicinity of a free surface are investigated. The results reveal that the velocity normal to the free surface is diminished, and the velocity components parallel to the free surface are enhanced in the region near the free surface. The magnitude of shear stress $\overline{uv}$ in the vertical central plane of the surface jet is smaller than that noticed in the free jet near the free surface, while the magnitudes of $\overline{uw}$ profiles are larger compared to that of the free jet. A higher magnitude of the vorticity is observed in the shear layers of the surface jet compared to that of the free jet. It is also noticed that the large-scale flow contributes the majority of U_{rms} as well as shear stress $\overline{uw}$, while the small-scale flow dominates the contribution of W_{rms}.

DEDICATION

To

My Motherland, China,

and

My parents and my wife

ACKNOWLEDGEMENTS

First of all, I would like to sincerely acknowledge my supervisor, Dr. Ram Balachandar, for his distinguished supervision and support. I also like to express my sincere gratitude to my committee members Dr. R. Barron, Dr. G. Rankin and Dr. Bolisetti for their helpful comments and suggestions.

Thanks to my parents and my wife who have supported me throughout my study.

Next I gratefully acknowledge Dr. V. Roussinova for her help and the endless discussions we have had to arrive with new ideas. Additional thanks to Mr. St. Louis, for his help and support in building and maintaining the experimental set-up.

Last but not the least, thanks goes to my best friends at the University of Windsor; Hengyu Qin, Xiaoshi Zhang, Jin Xu and Sara Liu.

TABLE OF CONTENTS

DECLARATION OF ORIGINALITY iii

ABSTRACT iv

DEDICATION v

ACKNOWLEDGEMENTS vi

LIST OF TABLES ix

LIST OF FIGURES x

NOMENCLATURE xiii

CHAPTER

I. INTRODUCTION

II. REVIEW OF LITERATURE

2.1 Characteristics of free jets 3
2.2 The behavior of confined jets 5
2.3 Coherent structures 7
2.4 Objective of present study 11

III. DESIGN AND METHODOLOGY

3.1 Experiment facility 12
3.2 Particle image velocimetry (PIV) system 17
3.3 Image processing 19
3.4 Proper orthogonal decomposition (POD) 20
3.5 Uncertainty analysis 22

IV. ANALYSIS OF RESULTS

4.1 Free jet characteristics 24
4.2 Surface jet characteristics 29
4.3 Vorticity of the jets 48
4.4 Proper orthogonal decomposition (POD) analysis 52

V. CONCLUSIONS AND RECOMMENDATIONS

5.1 Conclusions 65
5.2 Recommendations for future work 67

APPENDICES

Appendix A Uncertainty analysis 69

REFERENCES 74

VITA AUCTORIS 78

LIST OF TABLES

Table 3.1 Details of the measurement fields (*x/d* = 30 to 42)..... 15

Table 3.2 Details of the measurement fields (*x/d* = 42 to 62)..... 16

Table 4.1 Fractional energy contributions of the first 5 POD modes in horizontal planes53

Table 4.2 The number of POD modes used in the reconstruction to capture 50% TKE .. 56

Table A.1 Principal dimensions of target measurement 72

Table A.2 Uncertainty estimates from different sources for the instantaneous velocity .. 73

Table A.3 Summary of uncertainty of the instantaneous velocity..... 73

LIST OF FIGURES

Figure 1.1 Schematic of the vertical plane (*x*-*y*) of the surface jet 2

Figure 2.1 Schematic definition of a free jet..... 4

Figure 3.1 Schematic of the jet facility..... 13

Figure 3.2 Schematic of the nozzle..... 13

Figure 3.3 Location of field of views..... 14

Figure 3.4 Schematic of a typical PIV system..... 17

Figure 3.5 Schematic of image processing 20

Figure 4.1 Axial velocity and turbulence intensity near the jet exit (*x*/*d* = 0.2) 25

Figure 4.2 Normalized mean axial velocity profiles for a free jet..... 25

Figure 4.3 Decay of centreline velocity of a free jet in the axial direction..... 27

Figure 4.4 Half-width of a free jet in the horizontal central plane 27

Figure 4.5 Normalized mean streamwise velocity contour and vector profiles 28

Figure 4.6 Normalized mean streamwise velocity profiles in (a) Vertical central plane, (b) Horizontal central planes 30

Figure 4.7 Mean streamwise velocity profiles in the horizontal planes at *x/d* = 30, 45 and 60..... 31

Figure 4.8 (a) Normalized mean vertical direction velocity profiles in the vertical central plane (b) Normalized mean lateral direction velocity profiles in the horizontal central plane..... 35

Figure 4.9 Normalized mean lateral direction velocity profiles in the horizontal planes at *x/d* = 30, 45 and 60..... 36

Figure 4.10 Normalized mean streamwise turbulence intensity profiles in (a) Vertical central plane, (b) Horizontal central planes 39

Figure 4.11 Normalized mean streamwise turbulence intensity profiles in the horizontal planes at x/d = 30, 45 and 60 40

Figure 4.12 (a) Normalized mean vertical direction turbulence intencity profiles in the vertical central plane (b) Normalized mean lateral direction turbulence intensity profiles in the horizontal central plane..... 41

Figure 4.13 Normalized mean lateral direction turbulence intensity profiles in the horizontal planes at x/d = 30, 45 and 60 42

Figure 4.14 Normalized mean Reynolds shear stress profiles (a) $\overline{uv}/U_c^2$ in the vertical central plane (b) $\overline{uw}/U_c^2$ in the horizontal central plane..... 45

Figure 4.15 Mean Reynolds shear stress $\overline{uw}$ contours in the various horizontal planes at y/d = 0, ±2 and ±4 46

Figure 4.16 Normalized mean Reynolds shear stress ($\overline{uw}/U_c^2$) profiles in the horizontal planes at x/d = 30, 45 and 60 47

Figure 4.17 Average vorticity $\langle \Omega_y \rangle$ contours at 30 < x/d < 42 in the horizontal planes for free jet (first row) and surface jet (second row)..... 51

Figure 4.18 POD energy distributions in the horizontal central planes at 42 $\leqslant$ x/d $\leqslant$ 62 (a) Fractional contribution of each POD mode to the total energy, *Ei*. (b) Cumulative energy distribution, *En*..... 54

Figure 4.19 Vector plots of the fist 5 POD modes in horizontal central planes for free jet (first row) and surface jet (second row). 56

Figure 4.20 Example of instantaneous velocity field, (a) original fluctuating velocity field, (b) POD reconstructed large-scale velocity field and (c) residual velocity field..... 59
Figure 4.21 Streamwise turbulence intensity contours for free jet (first column) and surface jet (second column) 62
Figure 4.22 Lateral turbulence intensity contours for free jet (first column) and surface jet (second column)..... 63
Figure 4.23 Shear stress $\overline{uw}$ contours for free jet (first column) and surface jet (second column) 64

NOMENCLATURE

3-D	Three dimensional
B_u	Centreline decay rate
CCD	Charge coupled device
d	Nozzle diameter
d_{par}	Particle diameter
E_i	Fractional contribution of the energy of the i^{th} POD mode
E_n	Cumulative energy of the first n^{th} POD mode
FJ	Free jet
FOV	Field-of-view
F_r	Froude number
h	Depth of the jet
IA	Interrogation area
LDA	Laser-Doppler anemonetry
PIV	Particle image velocimetry
PLIP	Planar laser-induced fluorescence
POD	Proper orthogonal decomposition
$r_{1/2}$	Half-width of the jet
R_e	Reynolds number
SJ	Surface jet
U_c	Mean centreline velocity
U_e	Nozzle exit velocity
U_m	Maximum velocity

U, V, W	Velocity components in x-, y- and z- directions
$U_{rms}, V_{rms}, W_{rms}$	Root-mean-squared velocities in x-, y- and z- directions
$\overline{uv}, \overline{uw}$	Reynolds shear stress
x_0	Virtual origin
ZEF	Zone of established flow
ZFE	Zone of flow establishment
$\langle \Omega_y \rangle$	The normal component of the vorticity in x-z plane

CHAPTER I

INTRODUCTION

The study of turbulent characteristics of jets is of interest to engineers as they are used in various practical applications ranging from cooling surfaces to discharging wastewater into receiving waterbodies. Jets are also used in manufacturing processes and cleaning operations. While turbulence characteristics of unconfined (commonly termed as free) jets are well studied and documented (Wygnanski and Fiedler, 1969; Rajaratnam, 1976; Hussein *et al*., 1994), less is known about confined jets. When turbulent jets are discharged into a shallow environment, they can be vertically confined by both the free surface and solid boundaries. These confined jets are very complex and exhibit strong three-dimensional effects.

Confined jets can occur in the form of wall jets or surface jets where the confinement is from one side of the jet. For example, a jet developing near a solid wall is commonly termed as a wall jet and the flow is of infinite extent in the transverse direction, and unconstrained in either the streamwise or cross-stream directions (Launder and Rodi, 1983). Surface jets on the other hand are formed near the free surface where the confinement effect arises from a shear-free boundary. A sketch of a round jet in the vicinity of a free surface is shown in Figure 1.1. In contrast to free jets, the behavior of surface jets is influenced by the free surface.

In the present study, the modification of the jet characteristics due to the free surface interaction is studied experimentally. The velocity field is measured using a two-dimensional Particle Image Velocimetry (PIV), which provides instantaneous global velocity measurements with good spatial resolution. PIV measurements are obtained not

only in the central plane of the jet, but also in planes parallel to the free surface at various distances from the axis of the nozzle. The paper examines the modification of the mean velocity, turbulence intensity, and Reynolds shear stress fields caused by the interaction with the free surface.

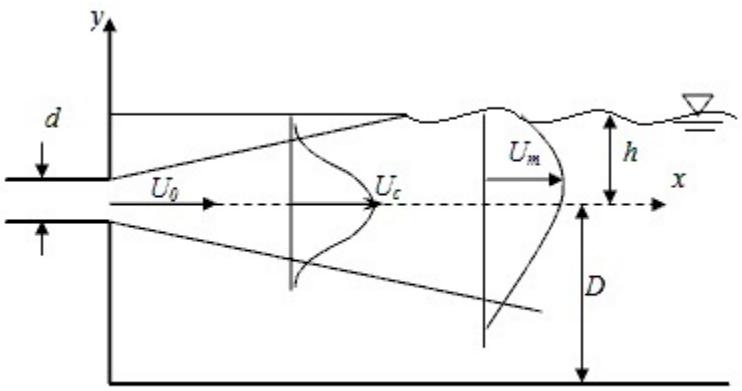

Figure 1.1 Schematic of the vertical plane (*x*-*y*) of the surface jet

CHAPTER II

REVIEW OF LITERATURE

A review of literature indicates that jets are of enormous interest to engineers and have been well studied. This chapter gives a brief review of the characteristics of free round turbulent jets. Followed by this, a review of the literature on the effect of boundedness on the jets is presented. In addition, a review of the definitions and characteristics of coherent structures in jets is provided.

2.1 Characteristics of free jets

The round free turbulent jet is geometrically the simplest case, which results when fluid has been issued from a round orifice into infinite space. The extensive literature and review articles available on round free turbulent jets provide fundamental knowledge (Abramovich, 1963 and Rajaratnam, 1976) about both jets and basic turbulence. Detailed description and analyses have also been presented by Wygnanski and Fielder (1969), Hussein *et al*. (1994), Xu and Antonia (2002), and Cenedese *et al.* (1994).

The development of a free jet is characterized by two regions: zone of flow establishment (ZFE) and the zone of established flow (ZEF) as shown in Figure 2.1. The distinguishing feature of ZFE is the presence of a potential core which is found to exist up to five or six nozzle diameters downstream of the nozzle exit. This is followed by the ZEF region farther downstream. For a free jet most of the studies have concentrated on the ZEF region. Many ZEF characteristics of a free jet have been reported by Wygnanski and Fiedler (1969). They showed that self-similarity is reached in steps and a jet is truly self-similar after approximately 70 diameters downstream of the nozzle. The mean velocity of the jet is self-similar at approximately 20 nozzle diameters downstream of the

nozzle, and the longitudinal fluctuations become self-similar approximately 40 diameters downstream of the nozzle, whereas the radial and tangential turbulence intensities attain similarity approximately after 70 diameters downstream of the nozzle. The flow can be presumed to be truly self-similarity only after that.

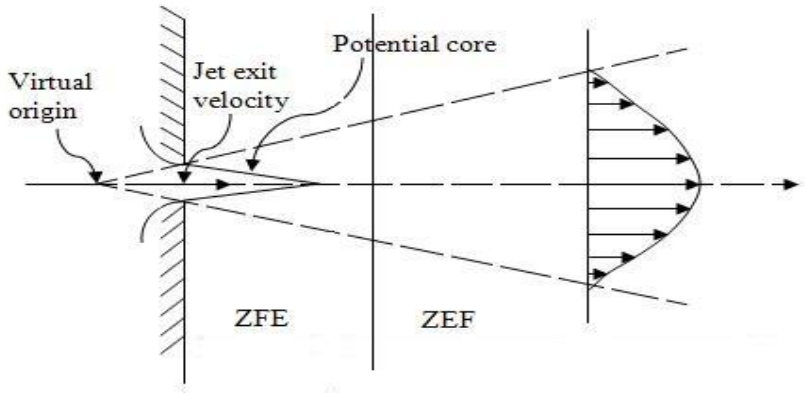

Figure 2.1 Schematic definition of a free jet

Hussain and Zedan (1978a, 1978b) found that the spread rate and peak turbulent intensity in the self-similar region depends on whether the initial boundary layer inside the nozzle is in laminar or turbulent state. The mean velocity and turbulence intensity profiles appear to reach self-similarity together when the initial boundary layer is laminar. In 1994, Hussein *et al.* reported measurements of the turbulent velocity field of a round jet to clarify the source of the discrepancy between previous studies. They used laser-Doppler anemometry (LDA) and both stationary and flying hot-wire (SHW and FHW, respectively) techniques for this investigation. It was argued that the far-field data of Wygnanski and Fiedler (1969) failed to satisfy conservation of momentum and concluded that the differences between the results reported by earlier investigators could be attributed to the smaller enclosures used in their studies and the recirculation pattern occurring within them.

Xu and Antonia (2002) made velocity measurements in two types of jets: the first, exiting from a smooth contraction nozzle and the second, from a long pipe with a fully developed pipe flow profile and compared several different velocity characteristics. The measurements in the contraction jet were in good agreement with the data of Hussein et al. (1994). The mean velocity and Reynolds stresses profiles indicate that the contraction jet develops more rapidly than the pipe jet, the former flow approaching a self-similar state more rapidly.

2.2 The behavior of confined jets

Contrary to an ideal situation involving free jets, in most of the engineering applications, jets tend to be under a confined condition. When turbulent jets are discharged into shallow environments, they can be vertically confined by both the free surface and the solid boundaries. Shallow jets are very complex and exhibit strong 3-D effects. A sketch of a round jet in the vicinity of a free surface is shown in Figure 1.1.

The earliest investigation of the interaction of a turbulent jet with a free surface is that of Evans (1955). When a jet interacts with a free surface, a surface current is formed which occupies a thin layer beneath the free surface. Although Evans (1955) did not study in detail the turbulent flow structures, the results show that when the surface waves and surface currents move in the same direction, the wave amplitude decreases and the wavelength increases. Rajaratnam and Humphries (1984) studied the mean velocity field of plane and circular turbulent surface jets where the free surface is located at the edge of the jet nozzle (h/d = 0.5 in Figure 1). They reported larger centreline velocities for the plane surface jet compared to that of the plane free jet. For a circular surface jet, the centreline velocity was found to decay faster than that noticed in the free jet.

Anthony and Willmarth (1992) studied the velocity and Reynolds shear stress characteristics of a turbulent jet issuing from a circular nozzle beneath and parallel to a free surface. The LDV measurements revealed that the maximum velocity is no longer at the jet centreline (as expected in the case of the free jet), but shifts toward the free surface with increasing distance downstream. Similar shift of the maximum velocity has also been observed by Madnia and Bernal (1994). Anthony and Willmarth (1992) noted that the turbulent fluctuations normal to the free surface were diminished, whereas those parallel to the surface were enhanced. The surface current that is formed propagates downstream and spreads laterally at an angle of approximately 40^o to the jet centreline. Madnia and Bernal (1994) also studied the interaction of a round jet with the free surface, but they were mainly concerned with the waves generated by this interaction at high Froude numbers. They also observed small-amplitude surface waves propagating at an angle of 42^o relative to the downstream direction.

Shinneeb (2006) investigated the effects of vertical confinement on a turbulent round jet discharging into quiescent shallow water at different degrees of vertical confinement. In his experiments, the jet characteristics were not only affected by the free surface but also by the proximity to the bottom impervious bed. The results showed that the axial velocity profiles in the vertical plane become almost uniform over the entire depth with a mild peak below the centreline of the nozzle. The axial velocity profiles measured in the horizontal plane continued to have a Gaussian shape. As the vertical confinement increased, the effect of the solid wall became more important with bed friction dominating the flow in the downstream sections. The turbulence intensities in both axial and vertical directions were found to be suppressed, but mildly enhanced in the

lateral direction. It was also observed that the Reynolds shear stress measured in the vertical plane was significantly reduced by the vertical confinement, while the Reynolds shear stress measured in the horizontal plane was only slightly affected. The study also showed that entrainment in shallow jets is suppressed in the vertical direction as the fluid is drawn from the lateral sides of the jet towards the jet centerline.

Sankar et al., (2005) investigated the interaction of a turbulent jet exiting from a square cross-section nozzle with a free surface. LDA measurements at various downstream locations showed that the top-hat velocity profile, close to the nozzle exit, gradually changes to a Gaussian profile further downstream. Once the jet starts interacting with the free surface, higher velocity was noticed closer to the free surface. The jet interacting with the free surface is no longer able to expand in the vertical direction and the free surface decreased the vertical jet spread and increased the jet spread in the transverse direction.

2.3 Coherent structures

It is now widely accepted that jets are characterized by large-scale coherent structures and understanding the physics of these structures is very important to study the characteristic features of turbulent jets. The existence of coherent structures has been known since the 1950's and were observed in shear flows by Brown and Roshko (1974). Even though extensive research work has been done in this area, no generally accepted definition of what is meant by coherent motion has emerged. A number of different definitions for coherent motion or coherent structures are available in literature (see Robinson, 1991). One restrictive definition is given by Hussain (1983), and he defines

coherent structure as a connected, large-scale, turbulent fluid mass with instantaneously phase correlated vorticity over its spatial extent.

A coherent structure originates from the instability of the shear layer. The structure can result from the instability of an initially laminar or turbulent or intermediate state. The coherent structure resulting from instability of laminar flows is quite periodic and repeatable in the early stages of formation. However, in fully developed turbulent shear flows there is a large dispersion in the shape, size, orientation, strength and convection velocity of the coherent structures and the structures have random trajectories (Hussain, 1983).

Coherent structures are spatially exclusive and cannot overlap; each structure has its independent domain and boundary. The interactions of coherent structures are intrinsically nonlinear, typically involving pairng or tearing. Pairing, including fractional pairing and partial pairing has been discussed by Hussain & Zaman (1981) and Hussain and Clark (1981). Pairing involves the amalgamation of two structures. Tearing occurs when a structure is torn into two or more parts. The process of vortex pairing and entrainment continues until the vortices are almost as large as the radius of the jet when circumferential instabilities set in and the vortices break down. The location of this breakdown coincides with the end of the potential core.

In general, vortical structures have a large dispersion in the characteristic parameters, such as shape, size, strength, orientation, convection velocity, etc. A coherent structure is usually recognized via vortical flow patterns, and the mode denotes the characteristic geometric configuration of the structure in the physical space. Hussain (1983) gives a few different modes, such as Hill's spherical vortex, hairpin vortex, vortex

ring, helical vortex, double helix, etc. If a mode is both dynamically significant and occurs frequently in a flow, this is called the “preferred mode” of the flow.

Although a coherent structure is characterized by high levels of coherent vorticity, coherent Reynolds stress, coherent production, and coherent heat and mass transport, it is not necessary for it to process a high level of kinetic energy. Most of the turbulent kinetic energy will be associated with incoherent turbulence. The energy content of coherent motion in jets is only about 10% of the total turbulent kinetic energy (Fiedler,1987). This makes the recognition of the structures difficult.

Extensive studies of coherent structures in the fully-developed turbulent axisymmetric jet have been made since coherent motion became a major focus of turbulence research. The jet becomes fully turbulent within about 70 diameters from the orifice, and it was believed that the spatial scales reduce as the vortex rings break up and are converted downstream. Dimotakis *et al*. (1983), using the Planar laser-induced fluorescence (PLIF) technique, inferred the presence of large-scale vortical structures in the jet far-field. They found evidence of both axisymmetric and helical modes, and proposed that the far-field of jets was an expanding spiral. Tso and Hussain (1989) conducted measurements in jets with a rake of X-wires and concluded that the helical mode is the most preferred and occurs 12% of the time. The double helical mode was found to occur 3% of the time. The ring mode, although present, was not considered to be dynamically important in the jet far-field. Dahm and Dimotakis (1990) reported that the instantaneous concentration field consisted of an ordered sequence of arrowhead shaped structures, with dimensions of the order of the local width of the flow in both directions, and also concluded the presence of ring and helical modes.

Agrawal & Prasad (2002) examined the organizational modes of the larger vortices educed from the low-pass filtered velocity data in the axial plane of a turbulent axisymmetric jet. The vortices were educed using a two-step process. First, a low-pass filtered field is obtained by convolving the instantaneous velocity field by a Gaussian kernel. Next, the low-pass field is Galilean transformed to expose the largest vortices. The advection velocity of these vortices is about 15% of the local mean centreline velocity. Ring and helical modes, and arrowhead shaped structures were evident after suitable combination of these operations. The diameter of the educed vortex ring is comparable with the local jet width, and its axis was aligned with the local instantaneous centreline velocity vector. The spacing between adjacent vortices for the helical coil increases with downstream distance, while the diameter was of the order of the local jet width indicating presence of an expanding spiral encompassing the jet body.

Shinneeb *et al.* (2008) investigated the coherent structures in the far-field region of an axisymmetric free jet using particle image velocimetry and the proper orthogonal decomposition method. The number of modes used for the POD reconstruction of the velocity fields was selected to recover 40% of the turbulent kinetic energy. The results clearly reveal that a substantial number of vortical structures of both rotational directions exist in the far-field region of the jet. The number of vortices decreases in the axial direction, while their size increases. The mean circulation magnitude is preserved in the axial direction. The results also indicate that the circulation magnitude is directly proportional to the square of the vortex radius and the constant of proportionality is a function of the axial location.

2.4 Objective of present study

The literature review has discussed the previous studies on the turbulent jet. The free turbulent jets have been investigated extensively, but the understanding of the surface turbulent jets is just how turbulence is generated at the expense of the mean motion. The review indicates that complete sets of turbulence quantities, e.g., the second-order stresses are scarce. The majority of coherent structures studies have been based on visualization and not on quantitative data. The present study will present a complete turbulent characteristic of the mean motion of the surface jet, such as mean velocity, turbulence intensities and Reynolds shear stresses. The study will also investigate the vorticity and coherent structures of the surface jets.

CHAPTER III

DESIGN AND METHODOLOGY

This chapter presents the details of the experimental setup and procedures used in the study. A detailed description of the Particle Image Velocimeter (PIV) used in the study along with typical uncertainty estimates is also presented.

3.1 Experiment facility

The experiments were conducted in a jet tank facility 2 m long, 1 m wide and 0.7 m deep as shown in Figure 3.1. This facility has been used in other similar studies (e.g., Tandalam *et al*., 2010). A circular nozzle was machined and mounted on the end wall of the tank, which was made of 0.75-inch thick aluminum plate. The nozzle itself was made of two arcs each of radius 10 mm and the nozzle exit opening is 10 mm in diameter (Figure 3.2).The centre of the nozzle was located 0.3 m above the bottom of the tank, and 0.5 m away from both side walls of the tank. The nozzle exit opening is flush with inside wall of the tank. The jet discharge was provided by an overhead reservoir with a constant head supply of 2.0 m. The flow from the overhead reservoir was controlled by a valve to deliver a constant velocity of 2.8 m/s at the nozzle exit. An adjustable downstream sharp-crested plate controlled the water level in the jet tank facility. In Figure 3.1, the origin of the coordinate system is at the centre of the nozzle exit and x is the axial direction along the flow direction. The vertical direction (normal to the free surface) is denoted as the y axis and it is positive upward while the lateral coordinate is denoted by z and the positive direction is defined according to the right hand rule.

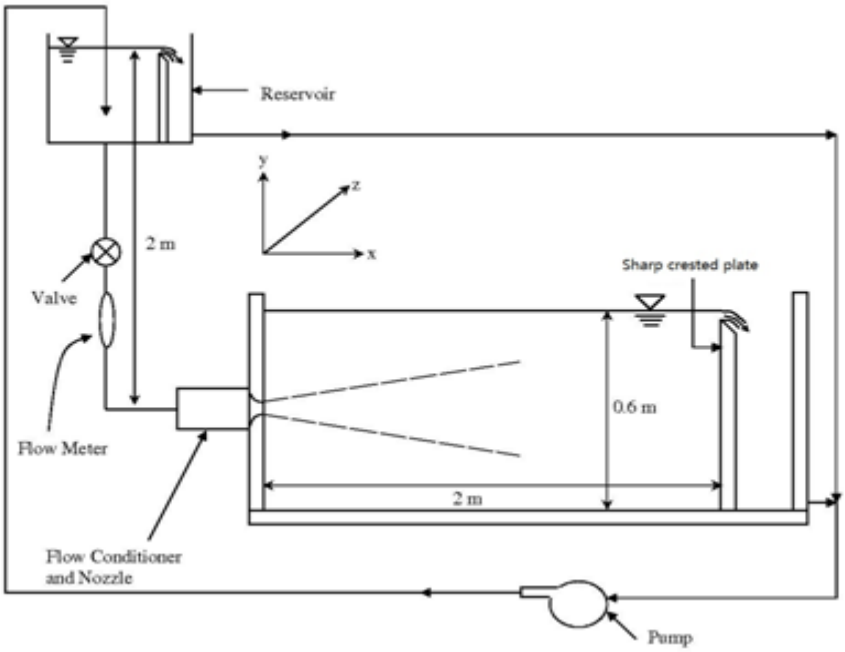

Figure 3.1 Schematic of the jet facility

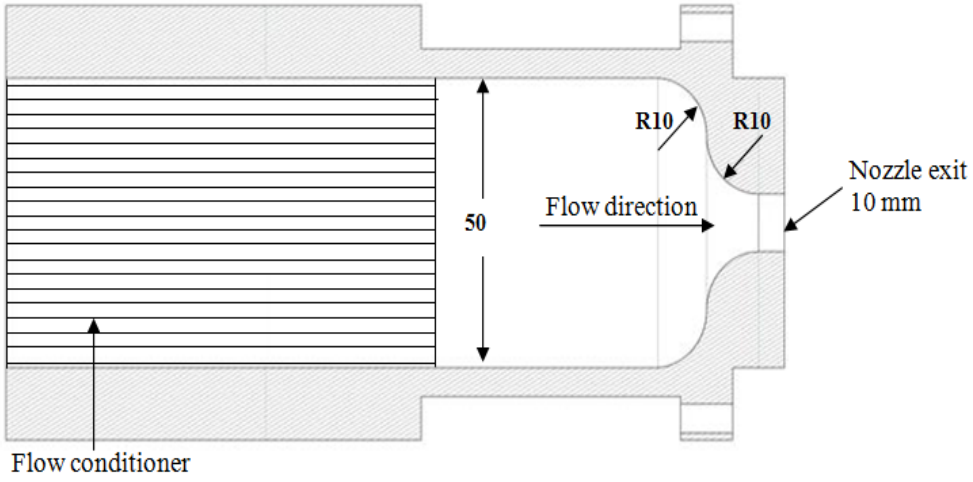

Figure 3.2 Schematic of the nozzle

The jet facility was operated at two different conditions depending on the jet submergence, *h/d*. Here, *h* denotes the vertical height of the water measured from the free surface to the centre of the nozzle, as shown in the schematics of Figure 2.2. While at *h/d* =30 the jet was expected to behave as a free jet, at a lower submergence *h/d* = 5, the jet is constrained vertically by the free surface and it is expected to behave as a surface jet. The Reynolds number based on the jet diameter (*d*) and exit velocity (U_e) for both jet conditions was kept constant $Re \equiv U_e d/\nu \approx 28{,}000$, and Froude number is $Fr \equiv U_e/(gh)^{1/2} \approx 4$ for the case of surface jet. Measurements were performed at vertical (*x*-*y*) and horizontal (*x*-*z*) central planes, and also several horizontal planes at various distances from the centreline (*y/d* = ±1, ±2, ±3, ±4) (Figure 3.3). The centreline of the jet is defined as a straight line passing through the axis of the nozzle and positive along the flow direction. The measurement fields-of-views (FOV) were roughly ranging from *x/d* = 28 to 62 in the streamwise direction. It will be shown later that $28 \leq x/d \leq 62$ corresponds to the region where the jet interacts significantly with the free surface at *h/d* = 5. The details of the experiments are tabulated in Table 3.1 and 3.2.

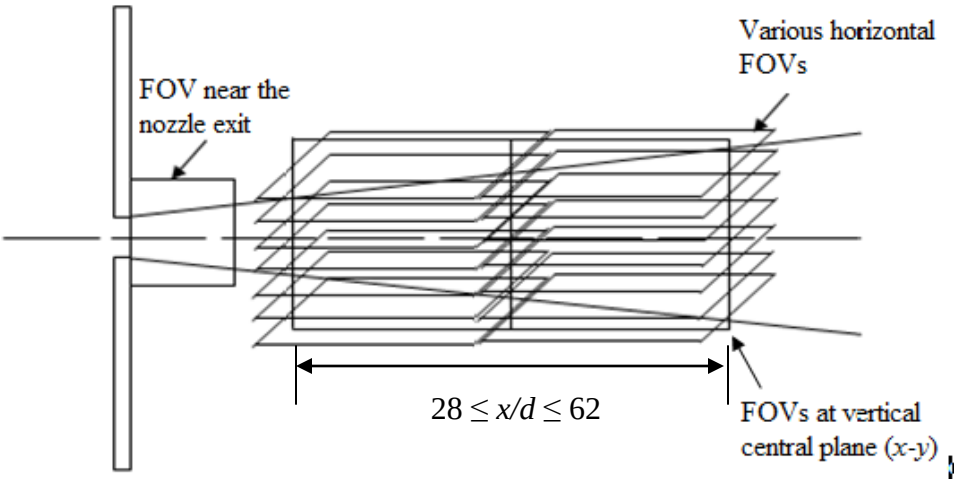

Figure 3.3 Location of field-of-views

Table A.1 Details of the measurement fields (x/d = 30 to 42)

	Case No.	Location	FOV (mm)	SOV (mm)
Free	FJ01	Vertical (z/d=0)	167	296
	FJ11	Horizontal (y/d=0)	147	289
	FJ12	Horizontal (y/d=+1)	149	288
	FJ13	Horizontal (y/d=+2)	151	287
	FJ14	Horizontal (y/d=+3)	153	286
	FJ15	Horizontal (y/d=-1)	145	290
	FJ16	Horizontal (y/d=-2)	143	291
	FJ17	Horizontal (y/d=-3)	141	292
Shallow	SJ01	Vertical (z/d=0)	167	296
	SJ11	Horizontal (y/d=0)	147	289
	SJ12	Horizontal (y/d=+1)	149	288
	SJ13	Horizontal (y/d=+2)	151	287
	SJ14	Horizontal (y/d=+3)	153	286
	SJ15	Horizontal (y/d=-1)	145	290
	SJ16	Horizontal (y/d=-2)	143	291
	SJ17	Horizontal (y/d=-3)	141	292

Table A.2 Details of the measurement fields (x/d = 42 to 62)

	Case No.	Location	FOV (mm)	SOV (mm)
Free	FJ02	Vertical (z/d=0)	169	455
	FJ21	Horizontal (y/d=0)	231	408
	FJ22	Horizontal (y/d=+1)	233	407
	FJ23	Horizontal (y/d=+2)	235	406
	FJ24	Horizontal (y/d=+3)	237	405
	FJ25	Horizontal (y/d=+4)	239	404
	FJ26	Horizontal (y/d=-1)	229	409
	FJ27	Horizontal (y/d=-2)	227	410
	FJ28	Horizontal (y/d=-3)	225	411
	FJ29	Horizontal (y/d=-4)	223	412
Shallow	SJ02	Vertical (z/d=0)	169	455
	SJ21	Horizontal (y/d=0)	231	408
	SJ22	Horizontal (y/d=+1)	233	407
	SJ23	Horizontal (y/d=+2)	235	406
	SJ24	Horizontal (y/d=+3)	237	405
	SJ25	Horizontal (y/d=+4)	239	404
	SJ26	Horizontal (y/d=-1)	229	409
	SJ27	Horizontal (y/d=-2)	227	410
	SJ28	Horizontal (y/d=-3)	225	411
	SJ29	Horizontal (y/d=-4)	223	412

3.2 Particle image velocimetry (PIV) system

Velocity measurements were carried out using a planar Particle Image Velocimetry (PIV) system. PIV is a non-intrusive technique to measure the flow velocity at multiple points simultaneously. A typical PIV system usually consists of several subsystems: a laser, a camera, and a synchronizer. Figure 3.4 briefly explains a typical setup for PIV measurement. Some specific tracer particles are added to the flow, and these are illuminated at a particular location twice within a short time interval by a laser sheet. Once the displacement of tracer particles within the time interval of the laser pulse is determined by some appropriate technique (for example, cross-correlation calculation), the velocity of each of the particles can be found by simply dividing the displacement vector by the already known time interval.

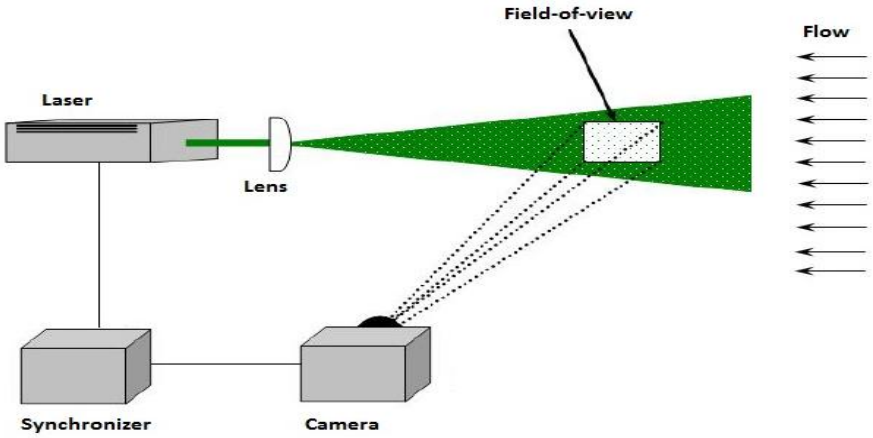

Figure 3.4 Schematic of a typical PIV system

The PIV technique does not measure the fluid velocity directly, rather it measures the velocity of the tracer particles. Thus, the properties of the tracer particle must be such that it would represent the fluid velocity in a satisfactory way. The particle should be big enough so that it can reflect enough light to be captured by the camera. On the other hand, it has to be small enough so that it can follow the flow velocity faithfully. Filtered water in the facility was seeded with 12 μm silver coated hollow glass spheres with a density of 1130 kg/m^3, The Stokes settling velocity of the particle can be estimated as (Clift et al. 1978)

$$u_s = \frac{g d_p^2 (\rho_p - \rho)}{18\mu}$$

Here, d_p is the particle diameter, ρ_p is the particle density and μ is the dynamic viscosity of the working fluid. Using this equation, the settling velocity was approximated as 0.01 m/s. This value is small enough to assume that the particles are capable of following the flow faithfully.

The seed particles were illuminated over a predefined FOV with overlapping laser light sheets. The laser light sheets were generated by a pair of Nd:YAG lasers beam with a maximum energy of 50 mJ per pulse at a wavelength of 523 nm and a pulse width of 10 ns passing through a combination of spherical and cylindrical lenses with focal length of 1000 mm and -15 mm, respectively. The thickness of the light sheet in the FOV was about 1 mm. To avoid the reflection of the laser sheet by the waves on the free surface, measurements were obtained only up to 4*d* above the central plane for the surface jet.

A high resolution Powerview Plus 4MP CCD camera [TSI Inc.] with a resolution of 2048×2048 pixels was employed to record pairs of time delayed images of the

particles. The camera was fitted with a Nikon 50 mm f/1.8 lens to best view the region of interest. 2000 images at a sampling rate of 1.04 Hz were obtained for each FOV.

3.3 Image processing

The image acquisition was performed with the software Insight 3G [TSI Inc.]. The total area of each raw image was divided into several small areas called interrogation area (IA). Typical IA size may be 16 × 16, 32 × 32 or 64 × 64 pixels. Either auto-correlation or cross-correlation method can be applied to the small IA to find the displacement of any particular particle in that interrogation area. If the time interval between these two images is known, the velocity vector can be determined as

$$V(\vec{x}, t) = \frac{\Delta S(x,\ t)}{\Delta t}$$

Where, ΔS is the displacement of the particle and Δt is the time interval between two successive laser pulses (Figure 3.5). In all experiments, the pair of images was first interrogated with an IA of 64 × 64 pixels using a Hart correlator. The particle displacements from the coarse grid interrogation were reanalyzed with a smaller 32 × 32 pixels interrogation area to improve the resolution and accuracy of the velocity field. At every stage, the interrogation areas were overlapped by 50%, and yielded a final velocity vector field of 127 × 127 vectors for each FOV. The spatial resolution of the processed velocity vector field is listed in Table 3.1. After the correlation analysis was complete, the invalid vectors were rejected by using the cellular neural network (CNN) method with a variable threshold technique proposed by Shinneeb *et al*. (2004). On average, the percentage of the valid vectors ranged from 90% to 94% minimizing the need to replace the rejected vectors with that calculated by using a Gaussian-weighted mean interpolation between the neighbours. The PIV data were further low-pass filtered with a narrow

Gaussian kernel with a width equal to two grid units ($2\Delta x$) to remove the noise due to the frequencies larger than the sampling frequency of the interrogation.

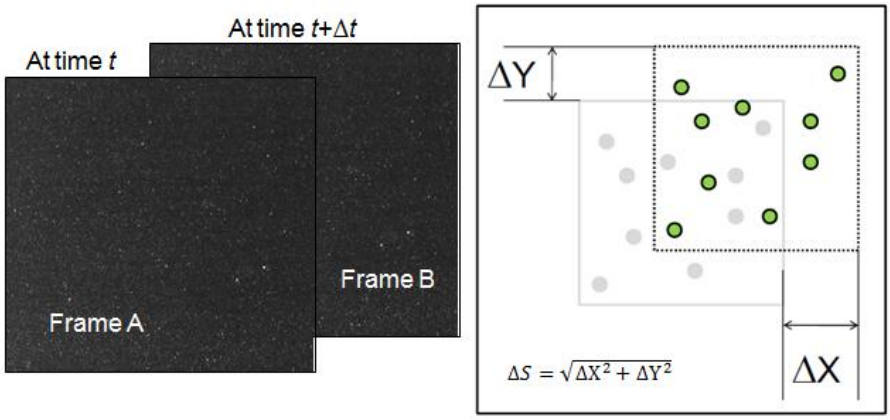

Figure 3.5 Schematic of image processing

3.4 Proper orthogonal decomposition (POD)

Proper orthogonal decomposition provides a basis for the modal decomposition of data obtained from experiments. POD was independently developed by several people (among the first was Kosambi in 1943) and finds uses in a variety of fields ranging from meteorology to image processing to chemical engineering. Berkooz et al., (1993) provides a comprehensive list of uses of POD. Depending on the field in which it is used, POD is known as Karhunen-Loeve decomposition, single value decomposition or principal component analysis.

POD was first introduced to the turbulence community by Lumley in 1967. It provides an optimal set of basis functions for an ensemble of data. It is optimal in the sense that it is an efficient way of extracting the most energetic components of a multi-dimensional process in only a few modes (Holmes et al., 1996). For most practical applications, the POD may be carried out using two methods: the direct method (Berkooz et al., 1993) or the snapshot method (Sirovich, 1987). Both methods were tested by

Graftieaux et al., (2001). There were no significant differences in the results the two methods yielded, the only differences noticed between the two were that the method of snapshots required smaller computation time and less memory consumption. In this study, the method of snapshots for POD as suggested by Sirovich (1987) has been used. A detailed discussion regarding the implementation of POD in order to extract coherent structures has been provided by Shinneeb (2006).

The method of snapshots POD procedure (Sirovich, 1987, Shinneeb, 2006) used for PIV data is summarized below:

The components of the correlation matrix are calculated by using the equation

$$C_{ij} = \frac{1}{M}\sum_{n=1}^{N}\mathbf{V}(\mathbf{X}_n,t_i)\,.\,\mathbf{V}(\mathbf{X}_n,t_j) \qquad i,j = 1\ldots\ldots\ldots M$$

where, M is the number of snapshots or PIV images, N is the number of vectors in a single snapshot and $\mathbf{V}(\mathbf{X}_n,t)$ is the instantaneous velocity vector at time t.

The eigenvalues and eigenvectors of the correlation matrix are calculated for the required number of modes.

The empirical eigenfunctions are then calculated using the equation

$$\mathbf{\Psi}_i^{(k)}(\mathbf{X}) = \sum_{n=1}^{M}\mathbf{\Phi}_n^{(k)}\mathbf{V}_i(\mathbf{X},t_n)$$

where, $\Phi_n^{(k)}$ is the n^{th} eigenvector of the k^{th} mode.

Knowing the eigenfunctions and instantaneous velocity sampled at a given frequency, the time-dependent coefficients, $a^{(k)}(t)$, of the POD can be calculated using the following equation:

$$a^{(k)}(t_l) = \frac{\sum_{n=1}^{N}\left(\mathbf{V}(\mathbf{X}_n, t_l).\boldsymbol{\Psi}^{(k)}(\mathbf{X}_n)\right)}{\sum_{n=1}^{N}\left(\boldsymbol{\Psi}^{(k)}(\mathbf{X}_n).\boldsymbol{\Psi}^{(k)}(\mathbf{X}_n)\right)}$$

Finally the reconstruction of the original PIV snapshots can be performed using the time dependent coefficients and the eigenfunctions in the following manner:

$$\mathbf{V}(\mathbf{X}, t_l) = \sum_{k=1}^{M} a^{(k)}(t_l)\boldsymbol{\Psi}^{(k)}(\mathbf{X})$$

3.5 Uncertainty analysis

The uncertainty of the PIV measurements is generally due to the particle inability to follow the fluid, timing precision, and error involved in the algorithm used to find the particle displacement. Since the particles are very small and their density is very close to the fluid density (low Stokes number), the error due to particle inability to follow the flow was considered negligible. The timing error was also found to be negligible since the delay generator and the laser pulse duration was controlled internally by the PIV electronics. The raw PIV images were analyzed prior to calculating the velocity vectors. The size of the particles in the individual PIV images was examined using Matrox Inspector software. According to Prasad *et al*. (1992), when the ratio of particle-image diameter to the pixel size is $d_{\text{par}}/d_{\text{pix}} > 3$ to 4, the uncertainty in the PIV displacement measurements is roughly 0.05 to 0.10 of the particle-image diameter. In the present study, the mean particle size has been found to approximate 3.2 pixels. The average particle displacement is about 6 pixels, resulting in a relative uncertainty of 0.8% to 1.7%. The random errors are minimal on the statistics of the velocity since large samples of 2000 image pairs were acquired at each measurement location with a relatively small sampling

rate of 1.04 Hz. The detail of uncertainty analysis is listed in Appendix A based on the guideline proposed by Visualization Society of Japan (VSJ, 2002).

CHAPTER IV

ANALYSIS OF RESULTS

This chapter presents the results the experimental study. One can recall that the jet diameter d and exit velocity U_e were 10 mm and 2.8 m/s, respectively, and the resulting Reynolds number $Re \equiv U_e d/v \approx 28{,}000$ and a Froude number $Fr \equiv U_e/(gh)^{\frac{1}{2}} \approx 4$ for the case of surface jet. The free jet characteristics are first discussed to evaluate the quality of measurements followed by comparison of free jet vs. surface jet characteristics.

4.1 Free jet characteristics

The first set of experiments were conducted at the jet submergence of h/d = 30 to access the quality of the experimental set up and procedures, and also acquire a set of data that will provide information about a free jet to enable direct comparison with a surface jet. Characteristics of the mean features of the jet, which include the jet exit properties as well as centreline velocity decay, the half width of the jet, the mean axial velocity fields in the downstream locations are discussed below.

Figure 4.1 shows the mean streamwise velocity and turbulence intensity profiles near the jet exit plane at x/d = 0.2, normalized by the jet exit velocity. The velocity profile is top-hat shaped and uniform across 85% of the nozzle exit section. The turbulence intensity is 0.7% in the core of the jet. The highest turbulence intensity is located at the edges of the jet (y/d = ± 0.5) where the shear layers are formed. The performance of the nozzle was evaluated against results from previous studies (Tandalam *et al*., 2010) which indicate that the nozzle and the flow conditioning system produced comparable uniform velocity distribution, low turbulence intensity jet flow at the exit. Mean streamwise

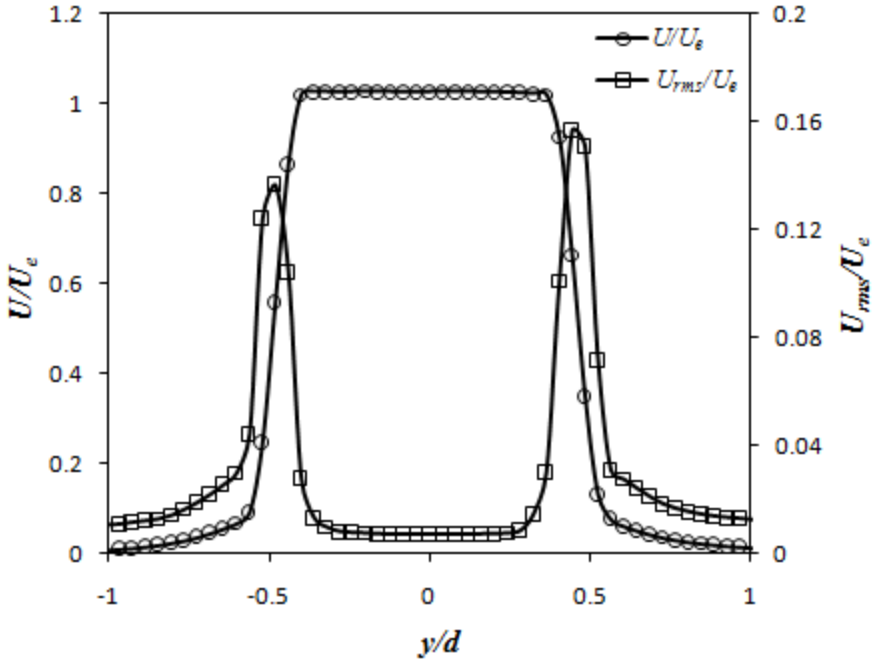

Figure 4.1 Axial velocity and turbulence intensity near the jet exit (x/d = 0.2)

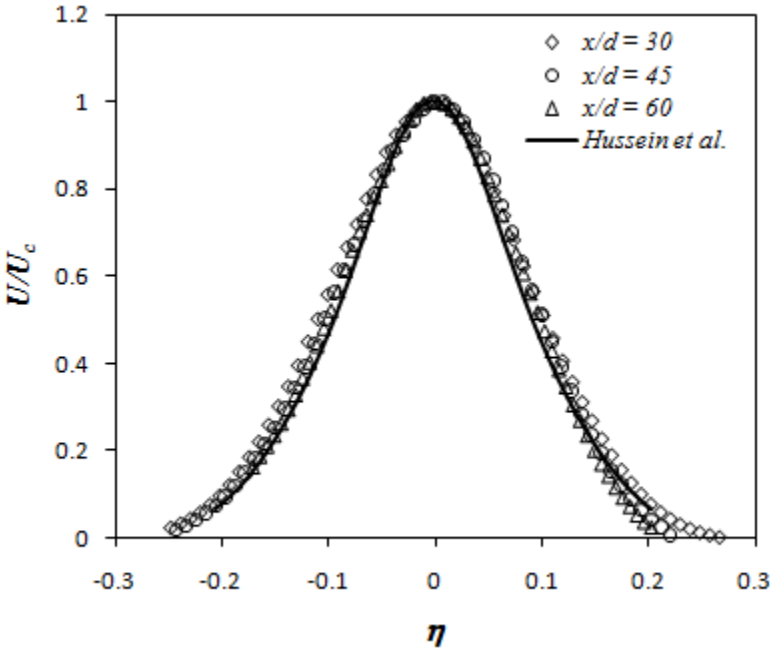

Figure 4.2 Normalized mean axial velocity profiles for a free jet

velocity profiles normalized by the jet centreline velocity U/U_c versus the non-dimensional coordinate, $\eta = y/(x - x_0)$ at downstream locations *x/d* = 30, 45 and 60 are shown in Figure 4.2. Here, x_0 refers to the distance from the virtual origin of the jet to the nozzle exit. The results of Hussein *et al*., (1994) have also been plotted in Figure 4 for comparison. All the velocity profiles are reasonably collapsed onto a single line, revealing the self-preserving nature of the free jet. The present data also show an excellent agreement with the data of Hussein *et al*. (1994).

The variation of the mean centreline velocity U_c is shown by plotting U_e/U_c as a function of the normalized axial location *x/d* in Figure 4.3.The figure shows that the mean centreline velocity decays linearly, but the slope of present measurement profile is slightly steeper than the result reported by Hussein et al. (1994). For an initial top-hat, self-preserving jet, the centreline velocity can be written as:

$$\frac{U_e}{U_c} = \frac{1}{B_u}\left(\frac{x}{d} - \frac{x_0}{d}\right)$$

Here, B_u is constant and x_0 represents the virtual origin. By modeling the centreline velocity according to above equation, one can calculate a decay rate of B_u= 5.4 and a virtual origin *x*/*d* = 7 for the present jet. This decay rate of 5.4 is comparable to the results are reported by other researchers which are in the range of 5.4 to 5.9.

It is hard to determine the jet spread rate by the outer boundary of the jet when the property exactly reaches zero. Therefore, it is common practice to quantify the spread of the free jet using the half-width of the jet, the radial location where the mean axial velocity is equal to half the centreline mean velocity of the jet. Figure 4.4 shows that the variation of the normalized half width $r_{1/2}/d$ with the normalized axial distance *x*/*d*. The

spread rate *Ks* of 0.104 is larger than 0.094 reported by Hussein *et al.* (1994), but it is in excellent agreement with 0.106 reported by Shinneeb et al. (2008).

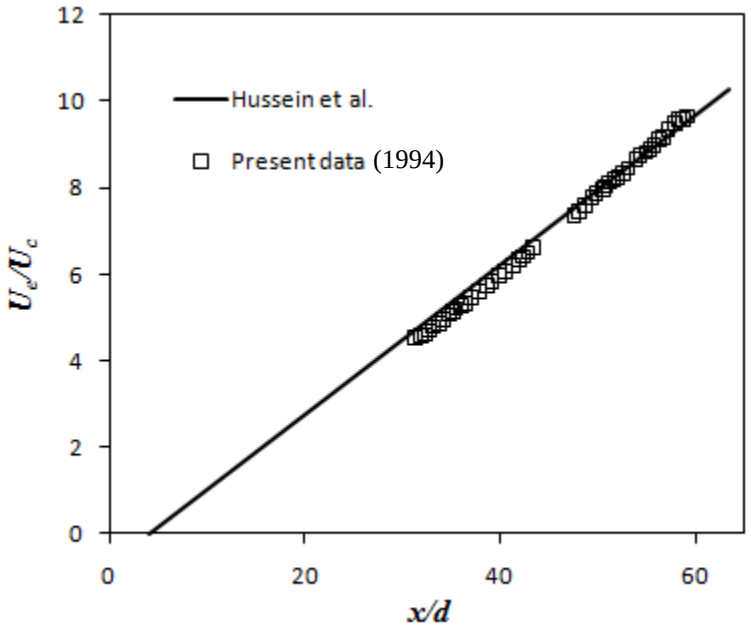

Figure 4.3 Decay of centreline velocity of a free jet in the axial direction

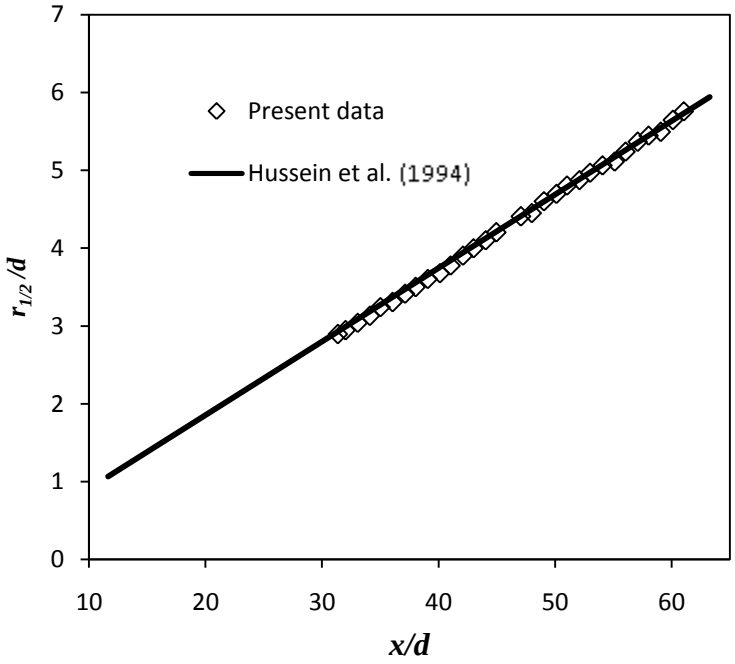

Figure 4.4 Half-width of a free jet in the horizontal central plane

The mean streamwise velocity contours normalized by the jet centreline velocity U/U_c at downstream distance from 30d to 60d are plotted in Figures 4.5a and 4.5b for the free jet and surface jet (denoted as FJ and SJ in forthcoming figures), respectively. In Figure 4.5a, as expected, at any axial station, the maximum values of the mean velocity is always located at the centre of the jet, and the vector profiles show the expected Gaussian shape. The free jet entrains the irrotational fluid and expands to about 10d at the downstream location x/d = 30. The velocity contours for the case of the surface jet are shown in Figure 4.5b. Since the free surface is located at 5d above the axis of the nozzle, it is expected that the jet will interact with free surface at a downstream location of $x/d \approx$ 30.

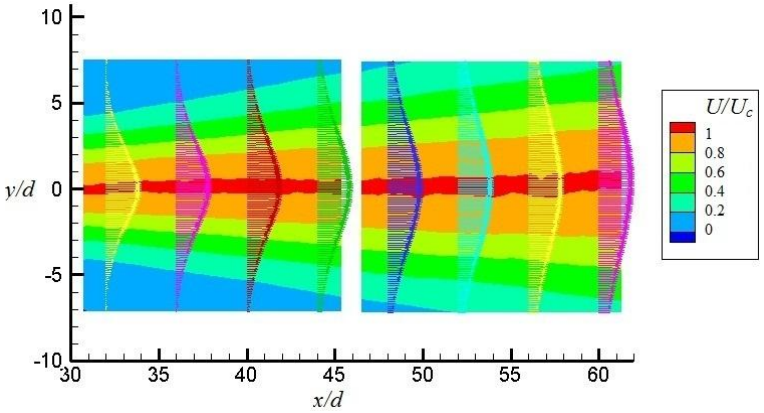

(a) Free jet

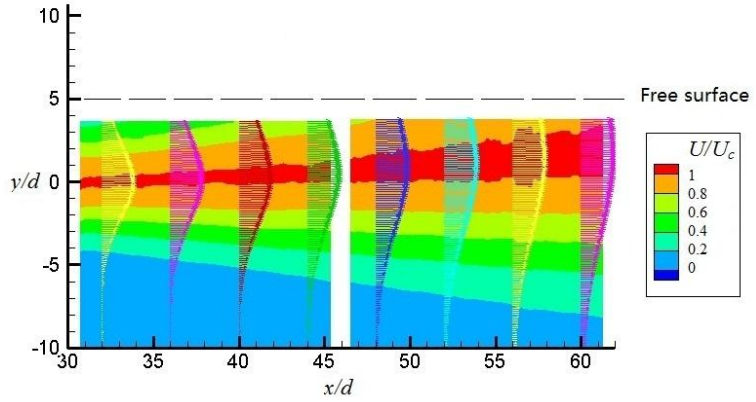

(b) Surface jet

Figure 4.5 Normalized mean streamwise velocity contour and vector profiles

4.2 Surface jet characteristics

Mean velocity and jet spreading characteristics

In Figures 4.6a and 4.6b, the normalized mean streamwise velocity profiles in the vertical (*x*-*y*) and horizontal (*x*-*z*) central planes of the surface jet are plotted, respectively. Free jet profiles (denoted by lines) at the same *x/d* locations are also plotted for comparison. The mean velocity is normalized by the local jet centerline velocity, U_c, whereas the vertical and lateral coordinates are normalized by nozzle diameter, *d*. The same normalization is used in all forthcoming figures. In Figure 4.6a, at $x/d = 30$, the shape and magnitude of the profile of the surface jet is very similar to that of the free jet. Because the jet just approaches the free surface, the effect of free surface confinement in the mean steamwise velocity is negligible. Although the left side of profile (the lower portion of the jet, $y/d < 0$) at $x/d = 45$ is also similar to the free jet profile, the right side of the profile (the top portion of the jet, $y/d > 0$) begins to deviate from the free jet profile. The maximum velocity is no longer located at y/d = 0, but it is located slightly towards the free surface. The magnitude of the mean streamwise velocity near the free surface is higher than that of the free jet. The difference between SJ and FJ become more significant at the farther downstream location $x/d = 60$. The profile of the surface jet is shifted towards the free surface. The magnitude of the velocity profile in the portion close to the free surface is much higher than that of the free jet. The velocity magnitude changes not only near the free surface but also in the lower portion of the jet where it becomes smaller than that of the free jet. This behavior of the surface jet is consistent with the results previously reported by Anthony and Willmarth (1992) and Madnia and Bernal (1994). In Figure 4.6b, unlike the profiles in the vertical plane, the mean

streamwise velocity profiles in the horizontal central plane (y/d = 0) at downstream locations x/d = 30, 45 and 60 are similar to those of the free jet with very small deviation.

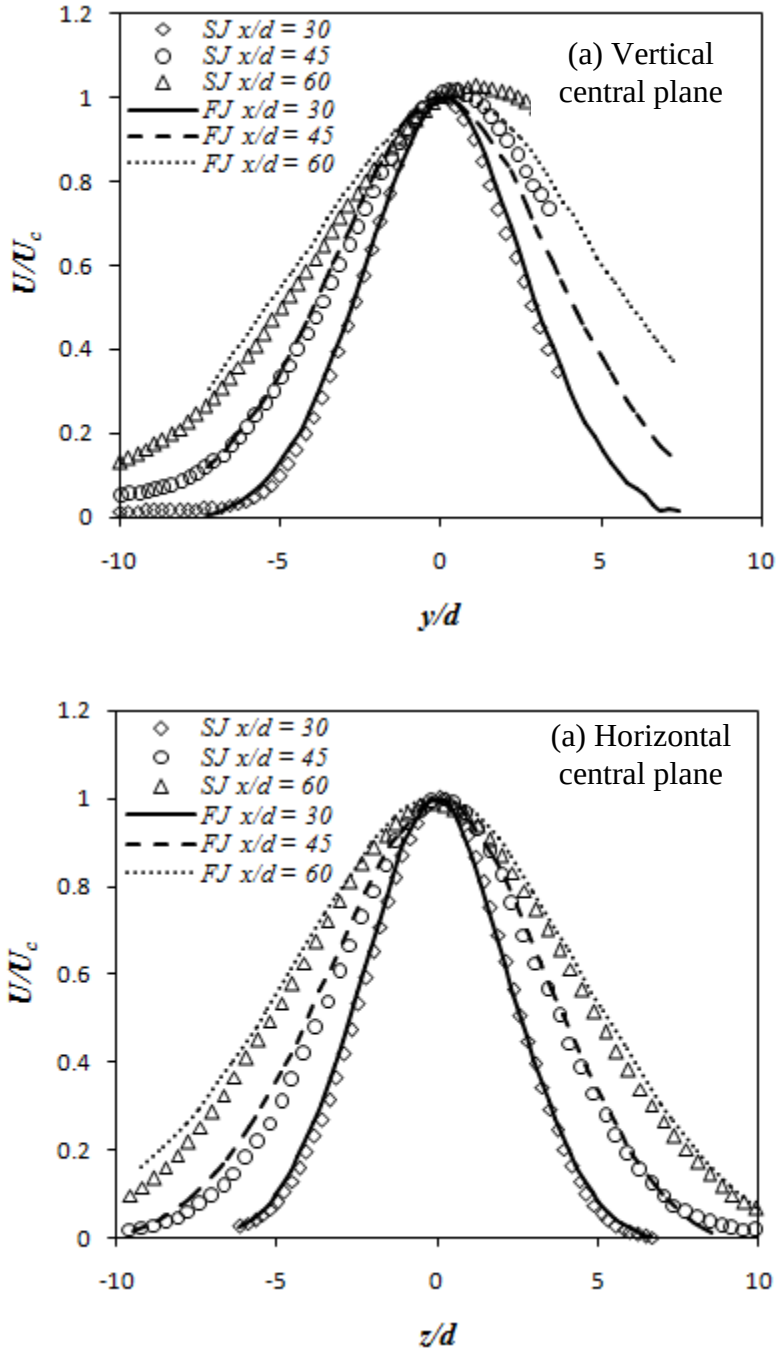

Figure 4.6 Normalized mean streamwise velocity profiles in (a) Vertical central plane, (b) Horizontal central planes

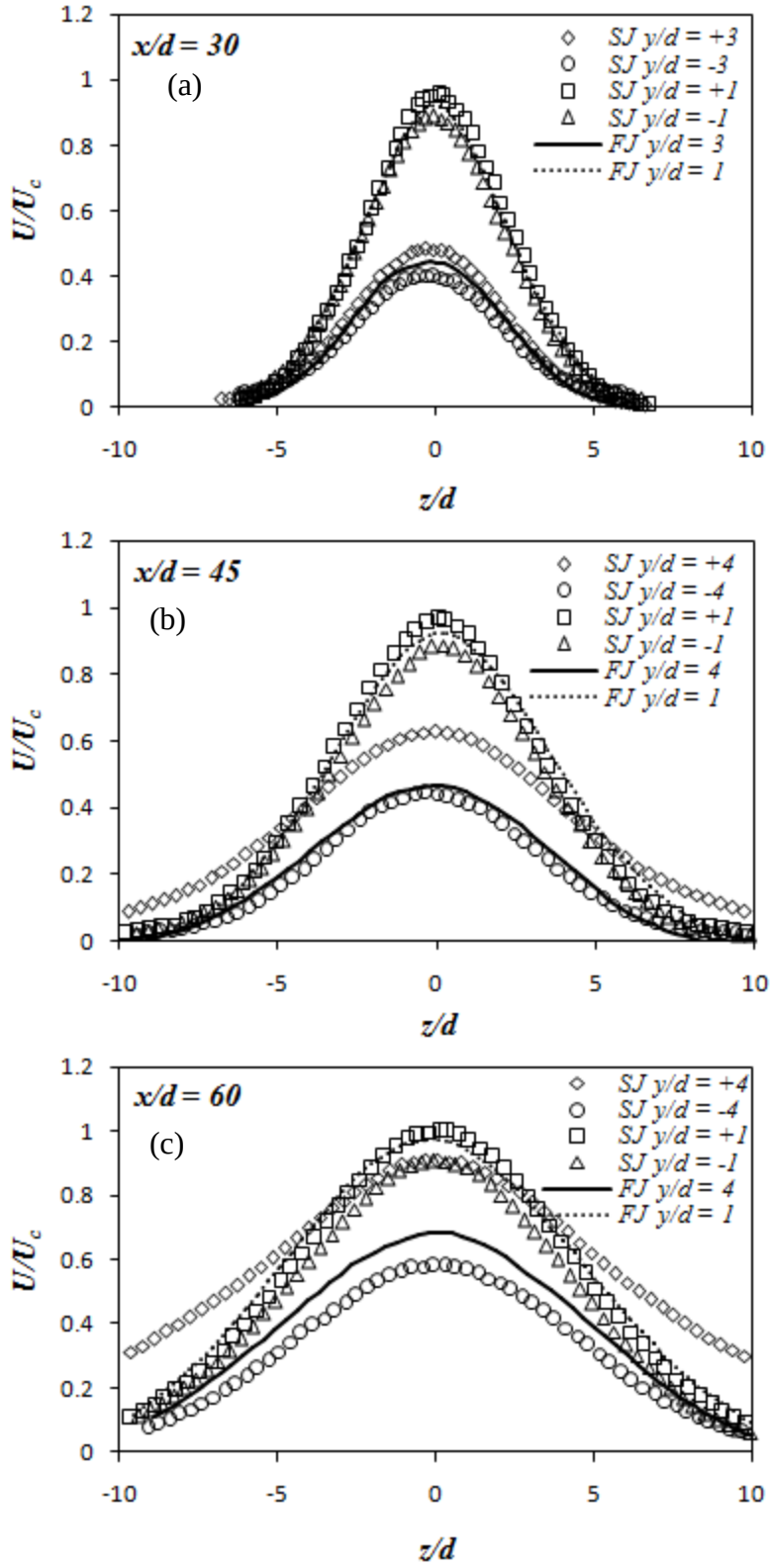

Figure 4.7 Mean streamwise velocity profiles in the horizontal planes at *x/d* = 30, 45 and 60

Although the streamwise velocity profiles in the horizontal central plane are similar to those of the free jet, differences are expected to occur in the profiles above and below the jet central plane. To examine this effect, PIV measurements were obtained in horizontal planes at various distances above and below the central plane for both free and surface jets. The mean streamwise velocity profiles in horizontal planes at x/d = 30, 45 and 60 are plotted in Figure 4.7. The free jet is axi-symmetric and as expected, the profiles at the same distance above and below the central plane were verified to be the same. In all forthcoming figures, for convenience, the profiles below the central plane of the free jet will be used to compare with the surface jet profiles. In Figure 4.7a, the SJ profiles at x/d = 30 are very similar to the FJ profiles with only slight difference in the middle region of the profiles. The free jet profiles appear to lie in between the surface jet profiles, with the SJ profile in the top region being higher than that of the corresponding location below the centre line. The overall characteristics of the surface jet are comparable to the free jet at this location. In Figure 4.7b at x/d = 45, the trend in the distributions are very similar to that noticed at x/d = 30, but the difference between the surface jet and free jet is more clearly visible, especially in the plane y/d = +4. The magnitude of the profile of surface jet is higher and wider than that of the free jet. The lower portion of the jet is not significantly affected by the free surface confinement which can be seen from the profile at y/d = -4 where there is a near overlap with the profile of the free jet. In Figure 4.7c, as the jet travels farther downstream, the profiles at plane y/d = +4 and -4 are distinctly different from those of the free jet. The profile at y/d = +4 is much wider, and velocity magnitudes higher than that of the free jet. However the profile at y/d = -4 is lower than that for the free jet. It should be noted that because the top

portion of the jet is unable to expand in the vertical direction, the jet experiences an asymmetrical entrainment. The consequences of this are reflected in the profiles.

The profiles of normalized vertical mean velocity (*V)* in the vertical central plane are shown in Figure 8a and the profiles of normalized lateral mean velocity (*W)* in the horizontal central plane are plotted in Figure 4.8b. Corresponding to the coordinate system adopted, on the right side of the profiles ($y/d > 0$ or $z/d > 0$), positive values of V or W indicate the outward growth of the jet and negative values indicated inward entrainment. The trend is opposite on the left side of the profiles ($y/d < 0$ or $z/d < 0$). In Figure 4.8a, the profiles for FJ and SJ are very similar in the lower portion ($y/d < -2$) at $x/d = 30$. The *V* component from this point upwards ($y/d > -2$) is clearly different in the two jets. A similar effect is also noticed at $x/d = 45$, but the region of overlap is limited to $y/d < -5$. With greater interaction occurring between the jet and the free surface at $x/d = 60$, the difference in the profiles between the free jet and surface jet is even more distinct. It should be noted that the lower portions of the jet are effected by the interaction with the free surface. In the case of the free jet, in the top portion of the jet, the upward vertical velocity component contributes to the expansion of the jet. The effect of the upward velocity component is reduced by the inward entrainment from the ambient flow above the jet. In the region close to the top edge of the jet, the vertical velocity component is directed downwards, because the region is dominated by inward entrainment. In the case of SJ, as the free surface is approached, the entrainment from the top of the jet is reduced, and the upward vertical velocity component occurring within the jet is not countered by an incoming entrainment. Consequently, the value of *V* is larger in the case of a surface jet. This can be seen from the profiles at $x/d = 30$ and 45, the magnitude of the velocity

in the middle regions of the profile is larger than those of the free jet. However, as the jet moves farther downstream, at x/d = 60, the jet fully interacts with the free surface, and it is unable to expand upwards. The overall vertical velocity is reduced significantly, and the magnitude of the profile is smaller than that of the free jet. In Figure 4.8b the trends of the profiles are very similar to the free jet, but the magnitudes are different at identical x/d stations. Clearly, the lateral entrainment of flow into the jet and the expansion of the jet are effected by confinement in the vertical direction.

Figure 4.9 shows the normalized lateral mean velocity profiles at various distances from central plane of the jet at x/d = 30, 45 and 60. In all figures, the differences between the free and surface jets at the sections away from the free surface (y/d = -4 and ±1) are negligible compared to the differences at the sections near to the free surface (y/d = +4 and +3). In Figure 4.9a, the profile at y/d = +3, the mean flow is inward everywhere across the profile. It should be noted that the measurement plane at this location is relatively far from the center of the jet and close to the edge of the jet. This region is dominated by the inward entrainment rather than outward growth in the center of the jet. As the jet interacts with free surface farther downstream (x/d = 45 and 60), the behavior of the lateral velocity component at the region close to the free surface gets changed. In Figure 4.9b, at y/d = +4, the mean flow tends to be outward everywhere. This behavior becomes more obvious at the downstream location x/d = 60. In Figure 4.9c, the magnitude of the profile increases dramatically compare to those in the lower planes. It reveals that the growth of the jet in the lateral direction is far greater than those of the plane below it. The increase of the magnitude of lateral velocity is accompanied also by

decrease of the vertical velocity component. As the entrainment of the ambient fluid is decreased in the upper regions of the jet, the overall jet flow re-adapts.

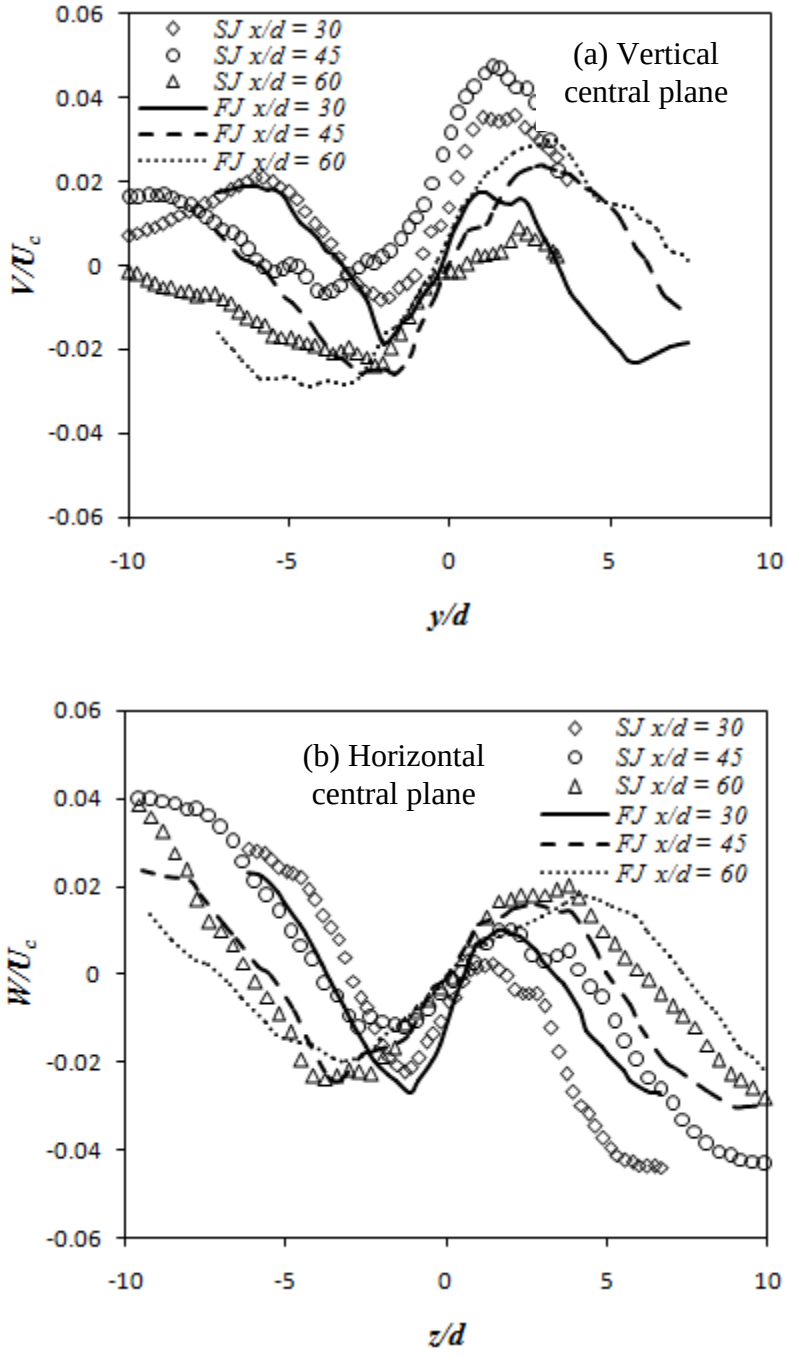

Figure 4.8 (a) Normalized mean vertical direction velocity profiles in the vertical central plane (b) Normalized mean lateral direction velocity profiles in the horizontal central plane

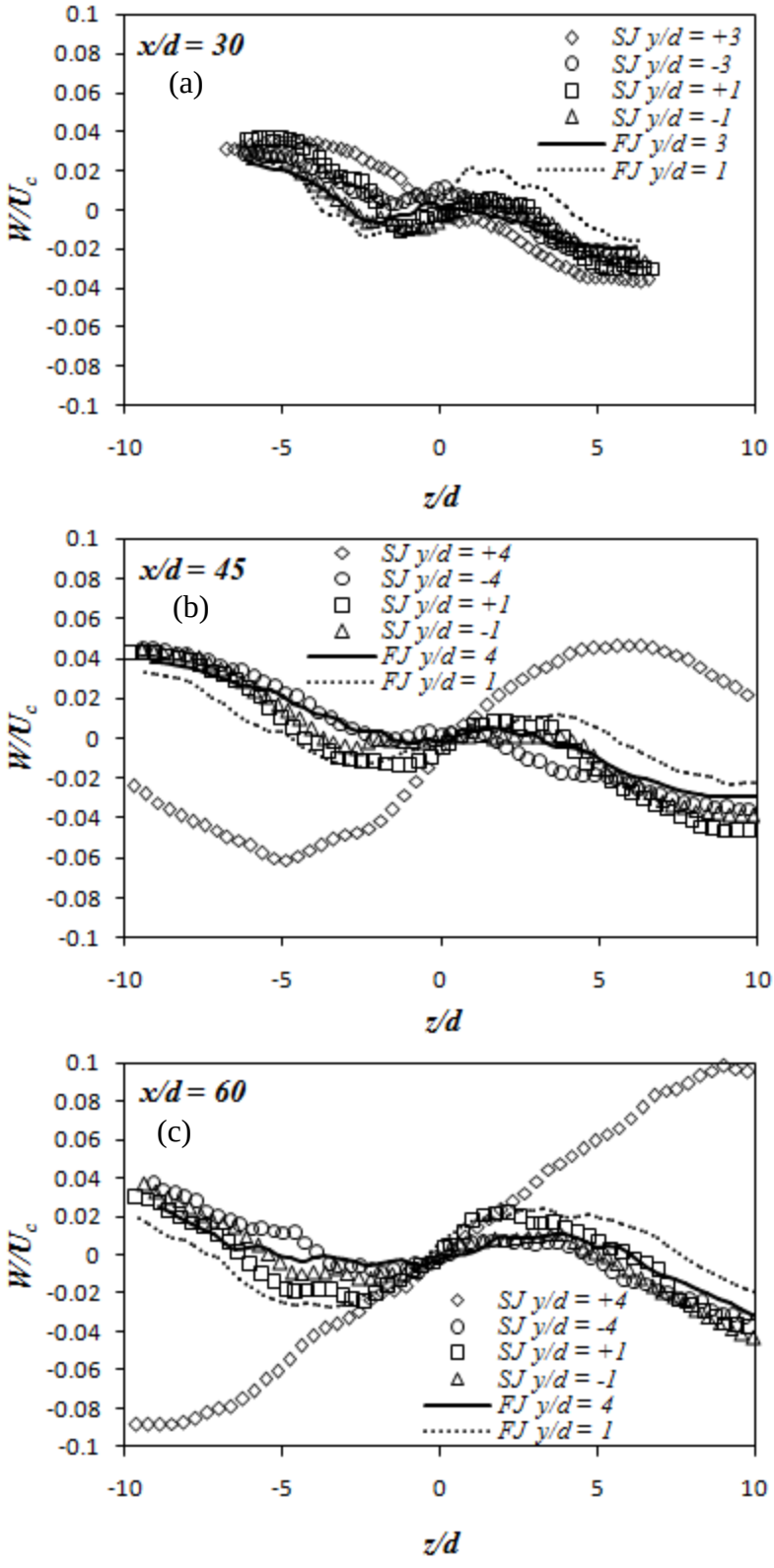

Figure 4.9 Normalized mean lateral direction velocity profiles in the horizontal planes at *x/d* = 30, 45 and 60

Turbulence intensity characteristics

Figures 4.10a and 4.10b show the streamwise turbulence intensity (U_{rms}) in the vertical and horizontal central planes, respectively. The profiles in the both vertical and horizontal central plane for the free jet and the surface jet are very similar in both shape and magnitude at x/d = 30. The profiles at this downstream location have typical off-axis double peaks. This is consistent with observations noticed in axi-symmetric free jets (Hussain, 1994; Shinneeb, 2006) at similar streamwise distances from the nozzle. With increasing downstream distance, the streamwise turbulence intensity of SJ is smaller in magnitude than that of FJ at identical x/d values in both vertical and horizontal central planes. This difference becomes even larger at the farther downstream location (x/d = 60). In Figure 4.10a, the profiles of SJ are not symmetrical and only one peak is found at y/d < 0. This is due to the presence of the free surface and the limitations in entrainment that occur from the top portions of the surface jet. In Figure 4.10b, in the case of free jet, at sections farther from the nozzle, the peaks are smoothened out to form a broader peak region in the central portion of the jet due to increased turbulence penetration of the jet by the entrained flow and the gradual development of a self-similar region which is expected to occur in the range of x/d = 70 for the free jet. This smoothening out of the peaks occurs much faster in the SJ profiles compared to the free jet.

Streamwise turbulence intensity in various off-axis horizontal planes for free and surface jets are shown at x/d = 30, 45 and 60 in Figure 4.11. For the free jet, as the measured planes are away from the central plane, it should be noted that a more complete penetration by external flow has occurred and the U_{rms} profiles exhibit a single peak. In Figure 4.11a, at x/d = 30, the effect of the free surface is mild in all planes with the FJ

profiles being reasonably close to the SJ profiles. Further, the SJ profiles at y/d = 1 and -1 are fairly similar. However, the U_{rms} values in the SJ profile at y/d = +3 are larger than the corresponding values at y/d = -1 in the upper portions of the jet. As the downstream distance increases, at x/d = 45, in Figure 4.11b, the profiles of the surface jet start to deviate from those of the free jet. At x/d = 60, the magnitudes of the profiles of the SJ are significantly smaller than those of the FJ as shown in Figure 4.11c. The significant decrease in the streamwise turbulence intensity is due to the reduced entrainment of the surface jet. Note that in Figure 11c, for y/d > -1, the turbulence characteristics of the surface jet changes and the off-axis double peaks re-appear. It reveals that the middle portion of this plane is dominated by the mean jet flow where the turbulence intensity is lower. This is consistent with the changes noted in the mean streamwise velocity profiles, which indicated that the mean flow of the jet shift towards to the free surface.

Figure 4.12a shows the normalized vertical turbulent intensity (V_{rms}) in the x-y plane, and Figure 4.12b shows the normalized lateral turbulent intensity (W_{rms}) in the y-z plane. For FJ, both the shape and magnitude of the V_{rms} profiles in Figure 4.12a are very similar to the W_{rms} profiles in Figure 4.12b as required by symmetry. This characteristic is not seen in the surface jet. It is not surprising that the both V_{rms} and W_{rms} profile of the surface jet collapse on to the profiles of the free jet at x/d = 30, because the free surface effect at this location is negligible. However, the SJ profiles at x/d = 45 and 60 are lower than that of FJ. In Figure 4.12a, in the region near the free surface, the profile shows a decreasing trend towards zero. In Figure 4.12b, the W_{rms} values of the surface jet is smaller than that of the free jet everywhere at x/d = 45 and 60. From the results discussed in Figures 10 to 12, it is clear that all three components of the turbulence intensity in the

surface jet are reduced due to the interaction with free surface, and this reduction is more visible as the downstream distance increases.

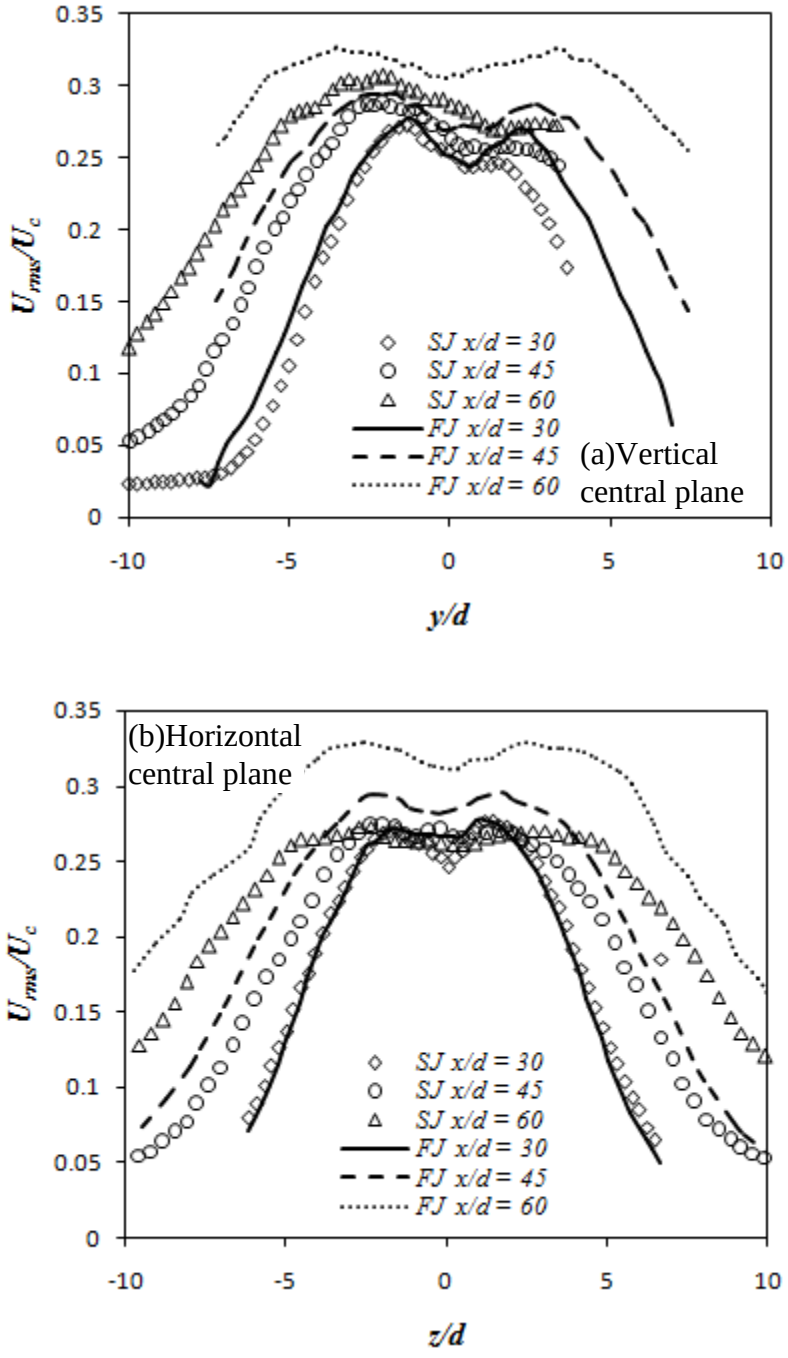

Figure 4.10 Normalized mean streamwise turbulence intensity profiles in (a) Vertical central plane, (b) horizontal central planes

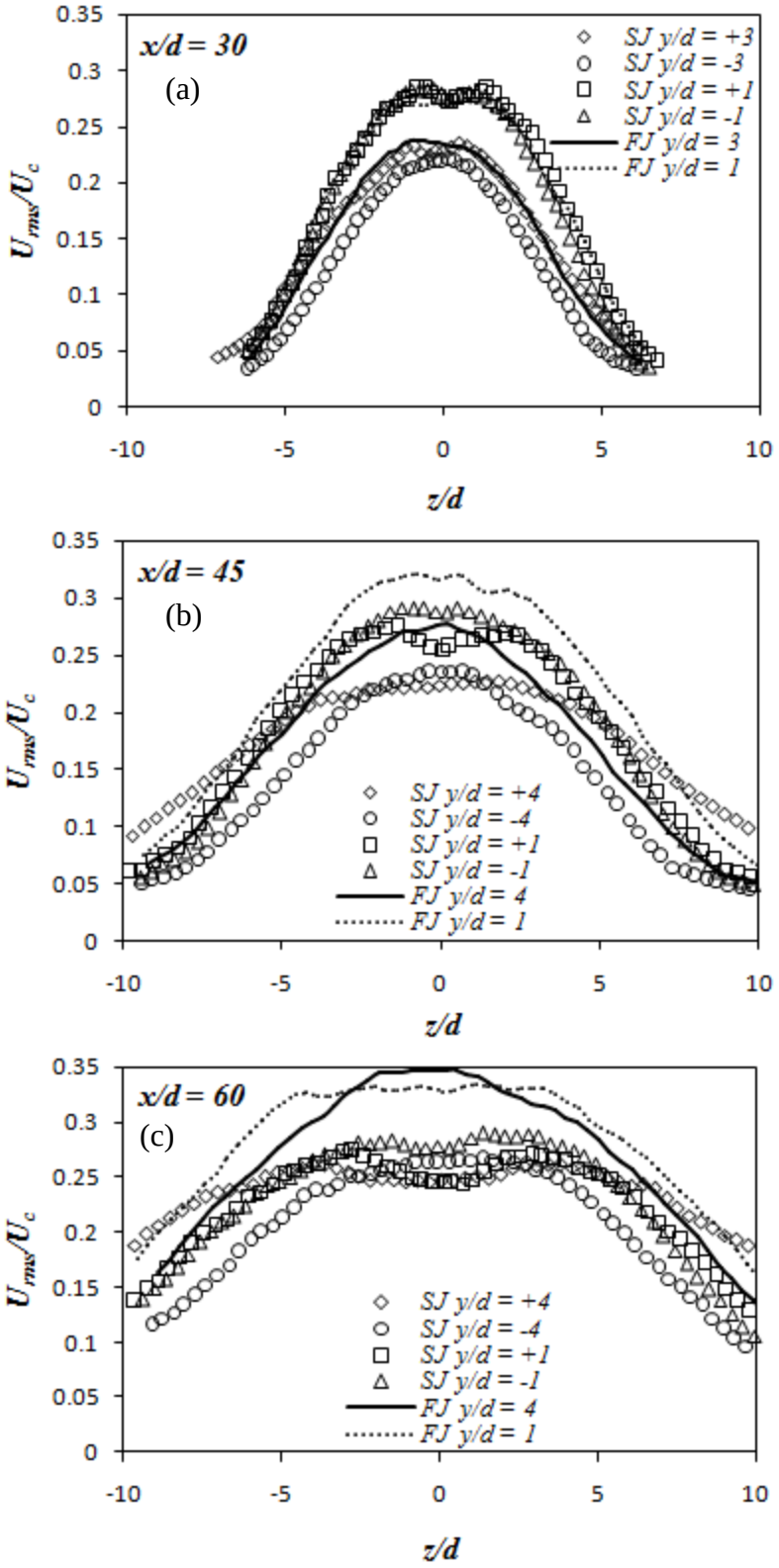

Figure 4.11 Normalized mean streamwise turbulence intensity profiles in the horizontal planes at x/d = 30, 45 and 60

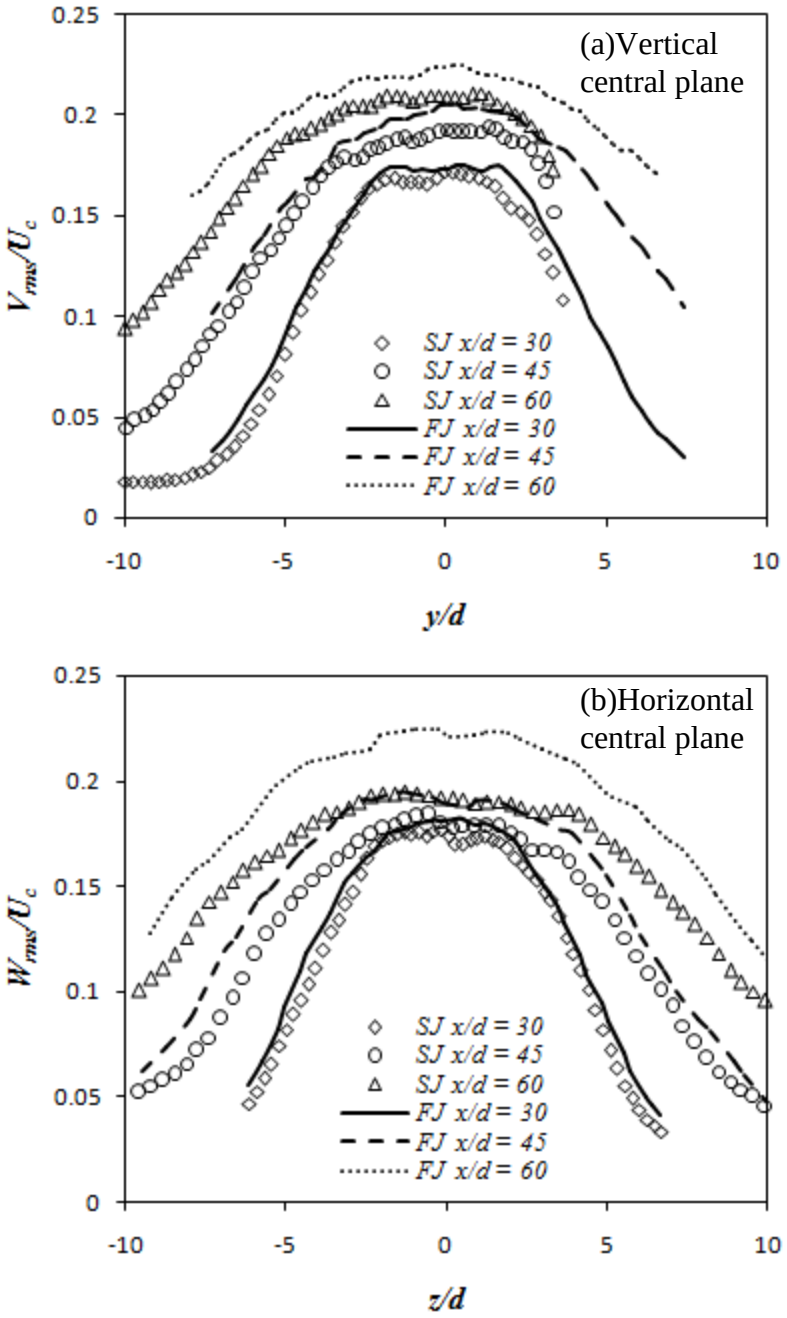

Figure 4.12 (a) Normalized mean vertical direction turbulence intencity profiles in the vertical central plane (b) Normalized mean lateral direction turbulence intensity profiles in the horizontal central plane

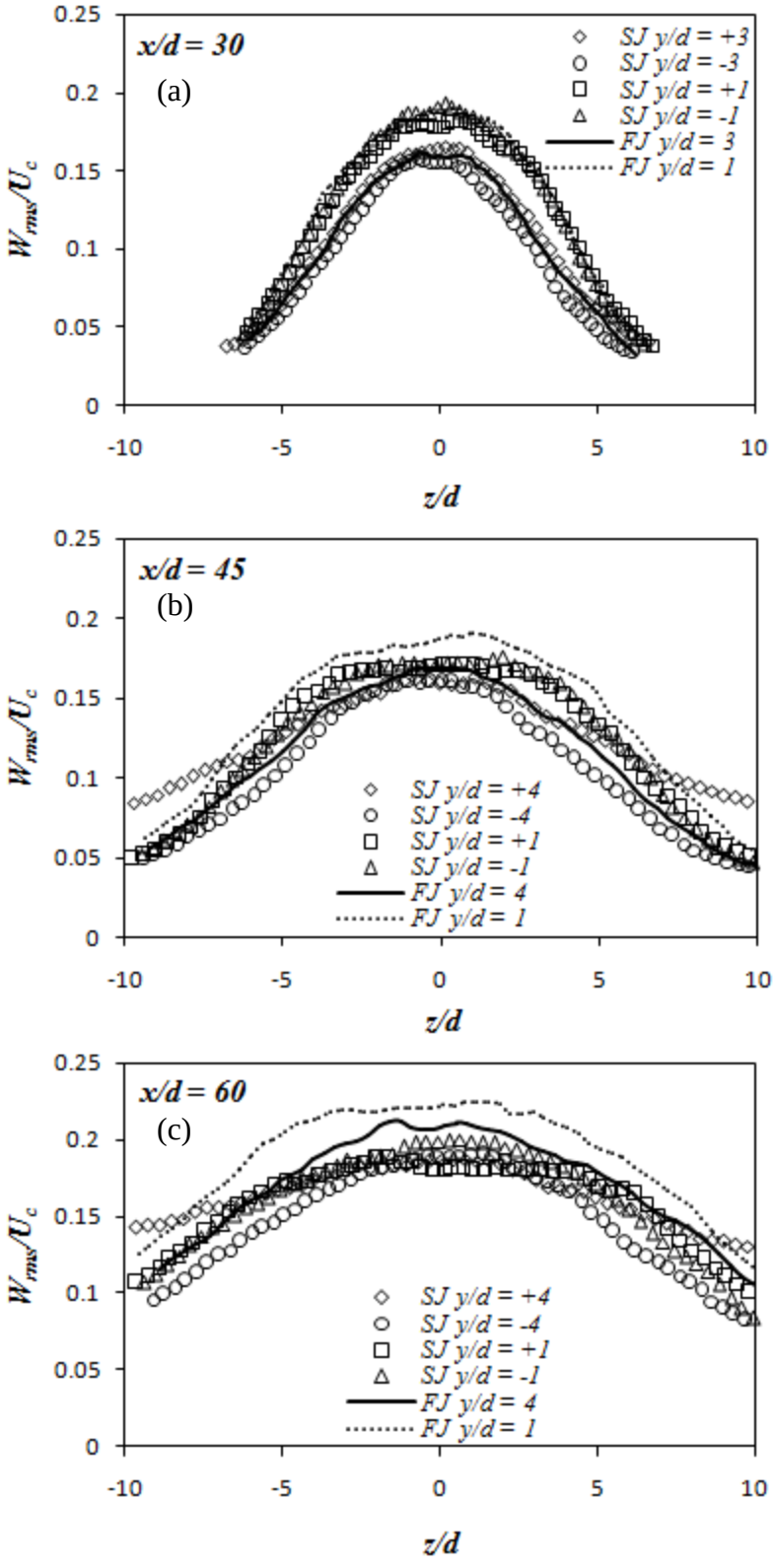

Figure 4.13 Normalized mean lateral direction turbulence intensity profiles in the horizontal planes at x/d = 30, 45 and 60

The lateral direction turbulence intensity in horizontal planes at *x/d* = 30, 45 and 60, are plotted in Figure 4.13 for the both SJ and FJ. Qualitatively, the trend in all planes is very similar to that in the horizontal central plane. The overall W_{rms} of the surface jet is smaller than that of the free jet when the downstream distance increases. In Figures 4.13b and 4.13c, it is noticed that the profile of the surface jet at *y/d* = +4 is wider than that of the free jet. The surface jet expands wider in this plane compared to the free jet. Therefore, the mixing region is relatively farther from the center of the plane.

Reynolds shear stress characteristics

In Figures 4.14a and 4.14b, profiles of the shear stress in the vertical and horizontal planes are shown as $\overline{uv}$ and $\overline{uw}$, respectively. The shear stress is normalized by the square of the centerline velocity. Both shape and magnitude of the free jet $\overline{uv}$ profiles in Figure 14a are similar to those of the $\overline{uw}$ profiles in Figure 4.14b. The peaks of shear stress are always seen in the shear layer regions, and the magnitude of shear stress is very similar on both sides of the centerline of the free jet as required by symmetry. In Figure 4.14a, for a surface jet, although the $\overline{uv}$ profile at *x/d* = 30 is very similar to the free jet, at *x/d* = 45 and 60, both shape and magnitude are different from that of the free jet. The shear stress in the region close to the free surface is much smaller than that of the free jet. The magnitude of the shear stress decreases with increasing downstream distance and it tends to be zero in the region close to free surface. This decreasing of shear stress is due to the significant drop in the both streamwise and vertical turbulence fluctuations, to satisfy the free surface condition. One can recall that in Figure 4.6a, in the region close to free surface, the value of streamwise velocity gradient along the vertical direction $\partial U/\partial y$ is smaller in the surface jet compared to the

free jet and it is negative. It is also noticed that in the same region $\overline{uv}$ is also smaller and positive in the surface jet. Therefore, the turbulence kinetic energy production term $-\overline{uv}(\partial \mathrm{U}/\partial \mathrm{y})$ has a positive value and is smaller in the surface jet compare to the free jet. This reveals that the turbulence kinetic energy is transferred from the mean flow to the turbulence, and that transferring of the energy is significantly reduced in the vertical plane by the free surface confinement. In Figure 4.14b, the shapes of the $\overline{uw}$ profiles of the surface jet and free jet are similar, but the magnitude is slightly smaller in surface jet. The difference in the $\overline{uw}$ profiles between the surface jet and free jet is not that distinct as the $\overline{uv}$ profiles found in Figure 4.14a. This is because the lateral direction is not constrained as the vertical direction, and the change in lateral component is not as much as the vertical component.

Figure 4.15 shows the shear stress $\overline{uw}$ contours in various horizontal planes. The results are presented in a dimensional form and are should recall that the nozzle exit velocity of the jet is the same for both free and surface jets. Figure 4.15a and 4.15b show the contours in the central plane for free and surface jets, respectively. Qualitatively, the figures are very similar except that the higher magnitudes in extend to a large *x/d* value for the surface jet. Figure 4.15c and 4.15d show the shear stress contours at $y/d = +2$. Clearly the magnitudes in the surface jet are higher than that in the free jet. This trend continue in Figure 4.15e and 4.15f at $y/d = +4$. It is clear that the effect of the free surface penetrate into the jet as the central plane ($y/d = 0$) shear stress contour in the surface jet are different from that of the free jet.

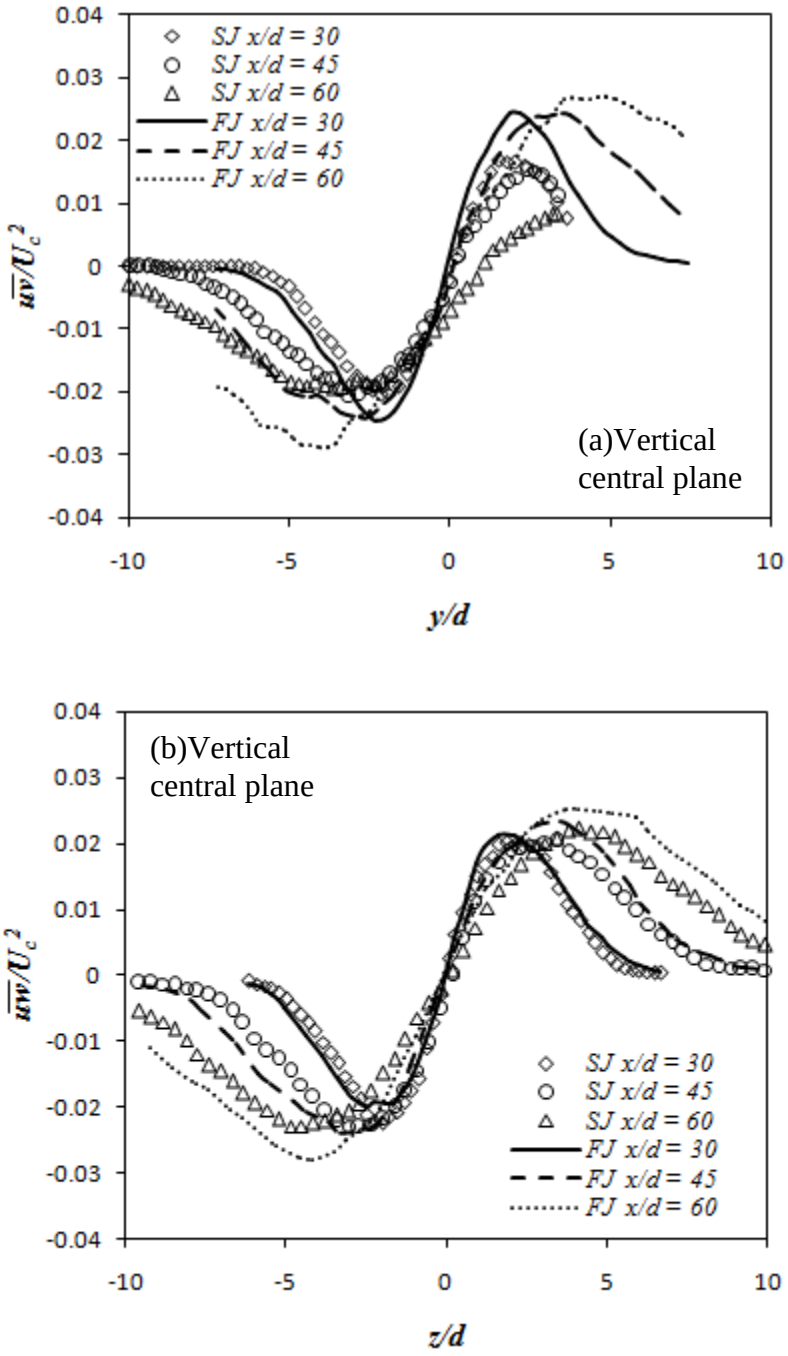

Figure 4.14 Normalized mean Reynolds shear stress profiles (a) $\overline{uv}/U_c^2$ in the vertical central plane (b) $\overline{uw}/U_c^2$ in the horizontal central plane

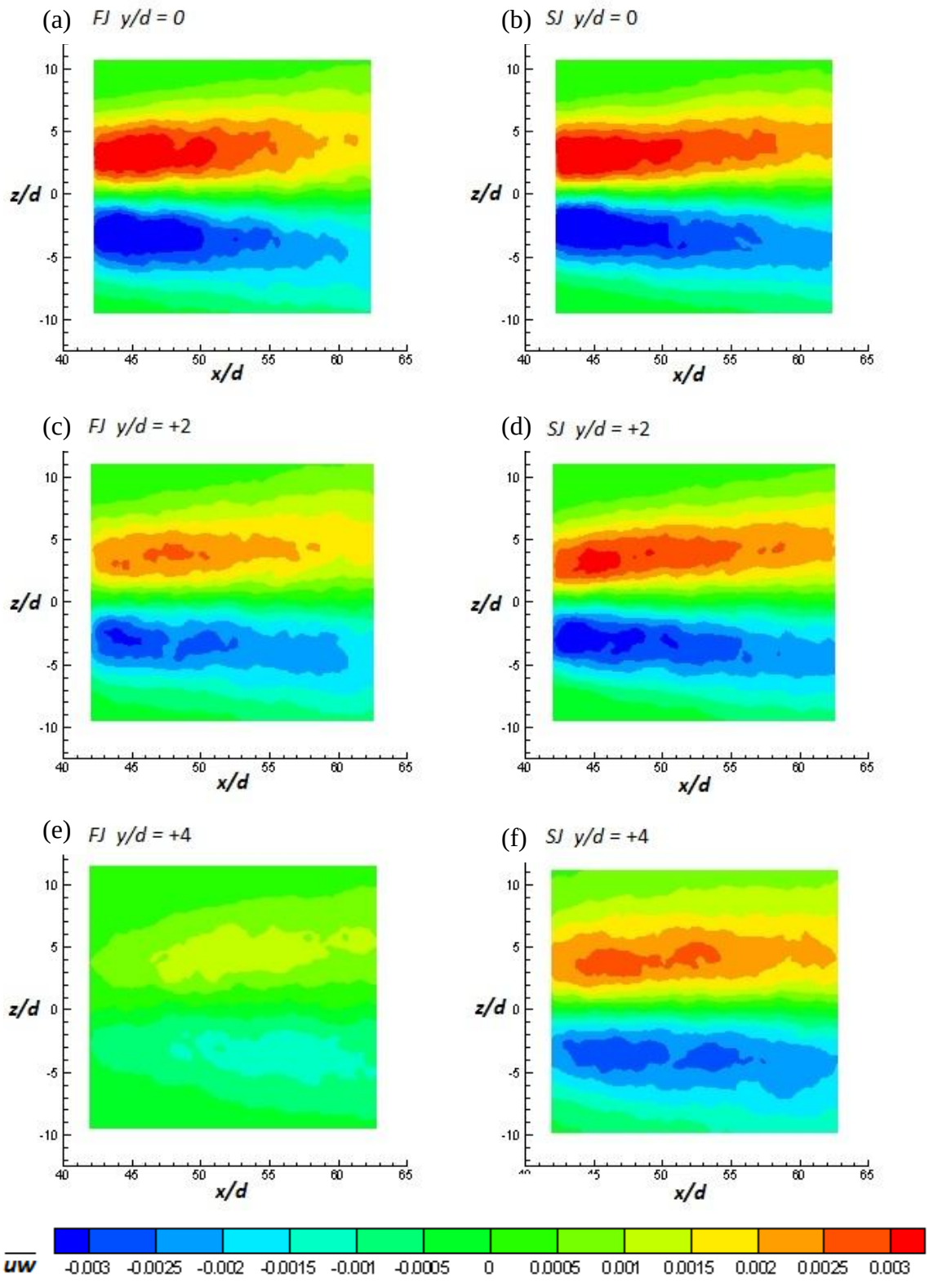

Figure 4.15 Mean Reynolds shear stress $\overline{uw}$ contours in the various horizontal planes at y/d = 0, ±2 and ±4

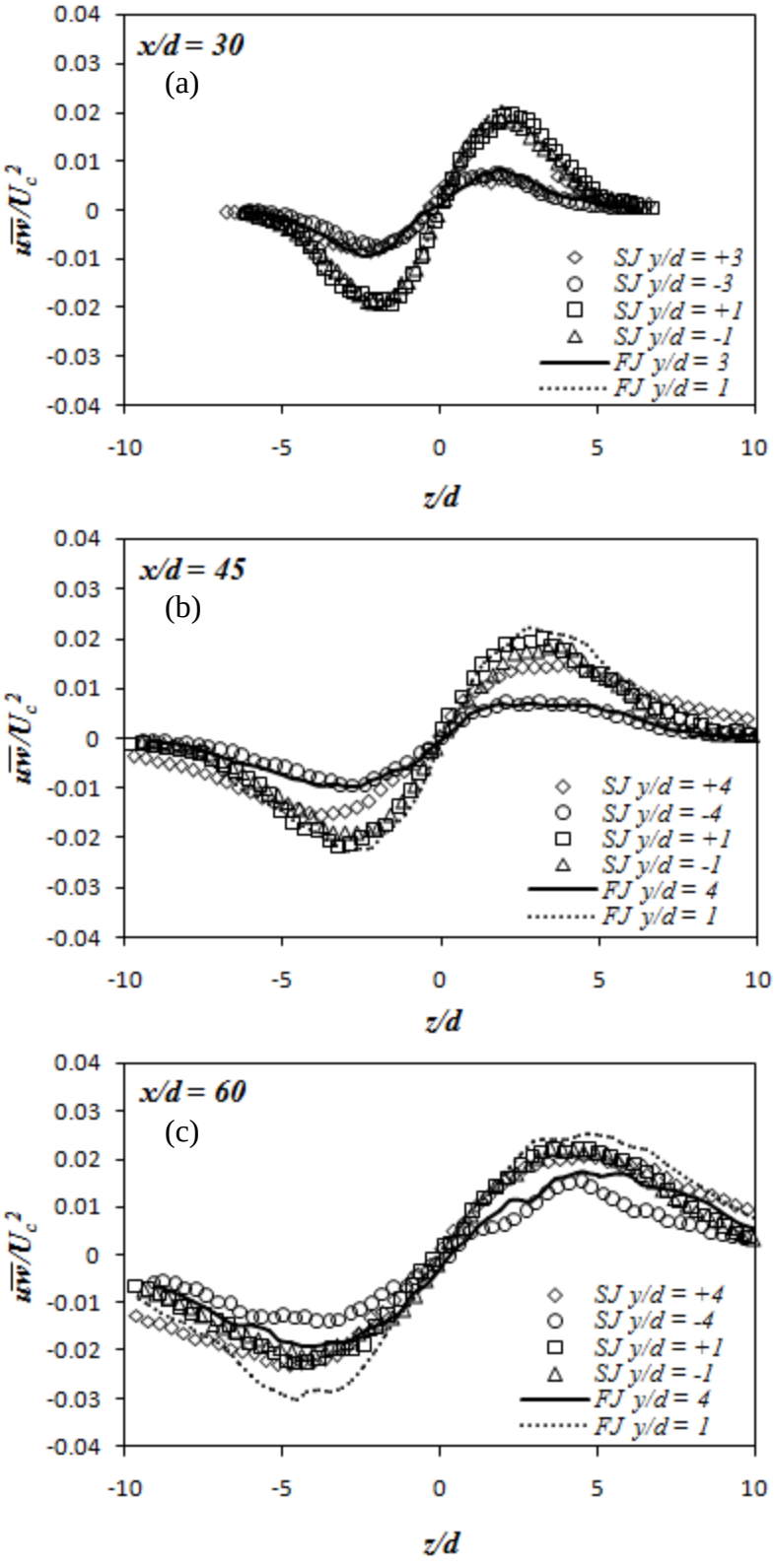

Figure 4.16 Normalized mean Reynolds shear stress ($\overline{uw}/U_c^2$) profiles in the horizontal planes at x/d = 30, 45 and 60

Figure 4.16 shows the $\overline{uw}$ profiles in horizontal planes at x/d = 30, 45 and 60. As the previous graphs, the results are presented in a non-dimensional form using U_c as the velocity scale. In Figure 4.16a, at x/d = 30, it is seen that the normalized $\overline{uw}$ profiles are comparable to those of the free jet. In Figure 4.16b and 4.16c, barring minor differences at $y/d = \pm 1$, the major the difference between the surface jet and free jet is seen at y/d = +4. It is interesting that the normalized magnitudes of the profiles at y/d = +4 are larger compared to that of the free jet at same location, but at the lower planes $y/d = \pm 1$ and y/d = -4, the magnitudes of the profiles is smaller than that of the free jet. It has been noticed that both U_{rms} and W_{rms} (see Figure 4.11b, 4.11c and 4.13b, 4.13c) are smaller in the surface jet in all horizontal planes. In the lower portion of the jet, the reduction in the shear stress $\overline{uw}$ is due to the reducing of turbulence. In identical horizontal planes, the shear stress ($\overline{uw}$) profiles are similar in both free jets and surface jets in regions where the interaction with the free surface is not significant ($x/d \approx 30$). As the downstream distance increases; near the free surface, the magnitudes of the shear stress profiles are larger compared to that of the free jet.

4.3 Vorticity of the jets

One of the advantages of the PIV measurements is the ability to capture instantaneous velocity measurements simultaneously at large number of points in different horizontal and vertical planes of the jet. In this study, the PIV yields a fairly dense instantaneous velocity field that can be characterized by flow quantities that require two velocity components (e.g., Reynolds stresses) or their derivatives (e.g., vorticity, swirling strength, etc.), that are usually not entirely accessible by other single point velocity measurement techniques. Most of the earlier classical jet studies (Wygnanski

and Fielder 1969 and Hussein et al., 1994) used limited number of probes and as such their results have limited spatial resolution. In the axisymetric jet, the vorticity is concentrated in the shear layers at the edges of the jet. Agrawal and Prasad (2002) documented that rotational motion induced by eddies residing in the shear layers of the axisymmetric jet is responsible for engulfing irrotational ambient fluid into the body of the jet. They have also shown that the profile of ensemble-average vorticity is symmetrical (with respect to the jet centreline) due to the inherent symmetry of the jet flow. Launder and Rodi (1980) analyzed the Reynolds equation for the streamwise vorticity of the axisymmetric jet and found that no streamwise vorticity is created in the round jet. However in the wall jet, application of the no-slip boundary condition at solid wall destroys this symmetry. Very few papers document the mean vorticity field of the free jet (Weisgraber and Liepmann, 1998) and there is no available data for the vorticity field of the submerged jet interacting with free surface. This section presents the average vorticity field analyzed in various horizontal planes in order to understand the motion of the coherent structures and their effect in the dynamics of the surface jet. Averaged vorticity fields are calculated by differentiating the instantaneous velocity fields using the Richardson extrapolation technique. In the horizontal planes, the normal component of the vorticity $\langle \Omega_y \rangle$ was calculated and contour plots are shown in Figures 4.17 for $30 < x/d < 42$. For comparison, contour plots of the free jet are also included in both figures. In Figure 4.17a and 4.17b, the mean vorticity $\langle \Omega_y \rangle$ contours are symmetrical in the central plane of the free and the surface jet ($y/d = 0$) with $\langle \Omega_y \rangle > 0$ in the radial half-plane $z/d > 0$ and $\langle \Omega_y \rangle < 0$ in the radial half-plane $z/d < 0$ with similar magnitude. Since

the free surface is located at y/d = +5, the normal vorticity in the central plane of the surface jet is not affected. The thickness of the shear layers at the edges of the surface jet are similar to those of the free jet with zero average vorticity along z/d = 0. Large magnitudes of $\langle \Omega_y \rangle$ are noticed at farther location in the FOV for the surface jet. In Figure 4.17c and 4.17d, the vorticit in horizontal planes farther from the jet central plane, are reduced in magnitude and the axisymmetric behavior of the free jet is maintained. For the surface and free jets no significant change of the vorticity was noted in the planes y/d = -3 (not shown here). The contour plot at y/d = +3 (Figure 4.17d) indicates a higher magnitude of the vorticity in the shear layers (at $z/d = \pm 3$) for the surface jet compared to that of the free jet (Figure 4.17b). This increase of the normal vorticity is a direct result of the reorientation of the vortices due to the confinement effect of the free surface. When the submerged jet interacts with the free surface, the structure of the jet is broken and smaller eddies contribute to the asymmetrical entrainment. Similar effect has been noted previously in the distribution of the mean velocity. A similar trend has been found at farther downstream locations $42 < x/d < 62$ (contours are not shown here). The increase of vorticity near the free surface is consistent with the increase of the Reynolds shear stress and supports the formation of the surface current observed by Anthony and Willmarth (1992).

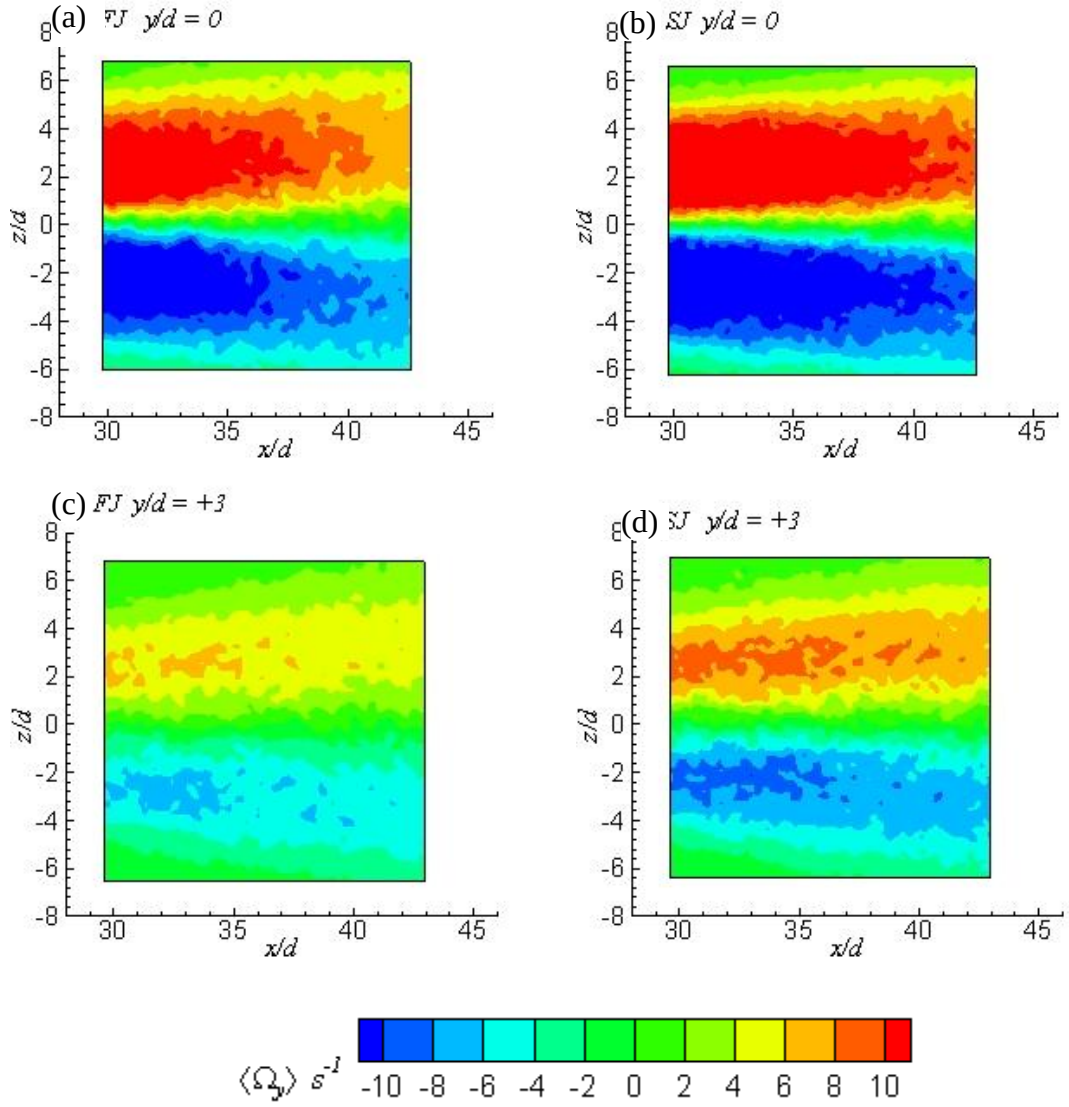

Figure 4.17 Average vorticity $\langle \Omega_y \rangle$ contours at 30 < *x/d* < 42 in the horizontal planes for free jet (first row) and surface jet (second row).

4.4 Proper orthogonal decomposition (POD) analysis

In this section, the POD analysis performed at the downstream location $42 \leq x/d \leq 62$ using 2000 instantaneous velocity fields for each horizontal plane is discussed. Table 4.1 presents the fractional contributions of individual POD modes to the total turbulent kinetic energy E_i for the first five POD modes in both free and surface jets. Lower order POD modes are representative of larger-scale features of the flow while higher-order POD modes correspond to smaller-scale and less energetic turbulent events (Holmes et al., 1996). It is noticed that the energy-contained in the first two POD modes are significantly larger than others, which indicates that the first two POD modes embody the largest scales of the flow. In addition, although the energy contained in specific modes are very different between the free and surface jet in most horizontal planes, it is very similar at the central plane ($y/d = 0$) for all 2000 modes. The energy-contained in the individual modes and cumulative energy of the modes of the central plane for both free and surface jet are presented in Figure 4.18a and 4.18b, respectively. When using POD to represent the flow field in turbulent flows, a majority of the total kinetic energy is contained within the first few POD modes. Generally a threshold, say 95%, of the total kinetic energy (TKE) is used and the mean flow is described by the first n POD modes, n being the minimum number of POD modes required to go above the specified threshold. All the POD modes above the n^{th} mode are considered to be part of the turbulent fluctuations. It should be noted that more than 400 modes are needed to capture 95% of the resolved TKE in the present free and surface jets. Thus, the present jets are quite complex owing to the wide range of dynamically important spatial scales presented. Figure 4.19 shows the contours of the first five modes for both the free and the surface

jet. It clearly shows that the patterns of the modes are very similar in the central plane for both the free and surface jet.

Table 4.1 Fractional energy contributions of the first five POD modes in horizontal planes

FOV (y/d =)	Modes n	1	2	3	4	5
+4	FJ	21.44	9.10	3.44	3.28	2.95
	SJ	12.80	11.48	4.61	4.37	3.20
+3	FJ	15.11	10.94	3.57	3.28	2.67
	SJ	14.17	8.84	4.73	3.23	3.12
+2	FJ	13.20	9.89	3.92	3.48	3.02
	SJ	13.99	6.83	4.71	3.41	3.10
+1	FJ	12.69	8.07	3.95	3.44	3.02
	SJ	13.53	4.55	4.54	3.59	3.33
0	FJ	12.69	5.24	4.29	3.69	3.15
	SJ	12.28	5.31	4.71	3.73	3.50
-1	FJ	14.43	7.59	4.01	3.37	3.01
	SJ	12.18	7.00	4.61	3.77	3.27
-2	FJ	13.04	11.54	3.70	3.60	3.01
	SJ	11.75	6.76	4.68	3.67	3.42
-3	FJ	18.02	10.62	3.59	3.34	3.05
	SJ	12.21	10.71	4.22	3.65	3.10
-4	FJ	18.71	10.36	3.38	3.32	2.88
	SJ	12.62	11.17	4.31	3.88	3.38

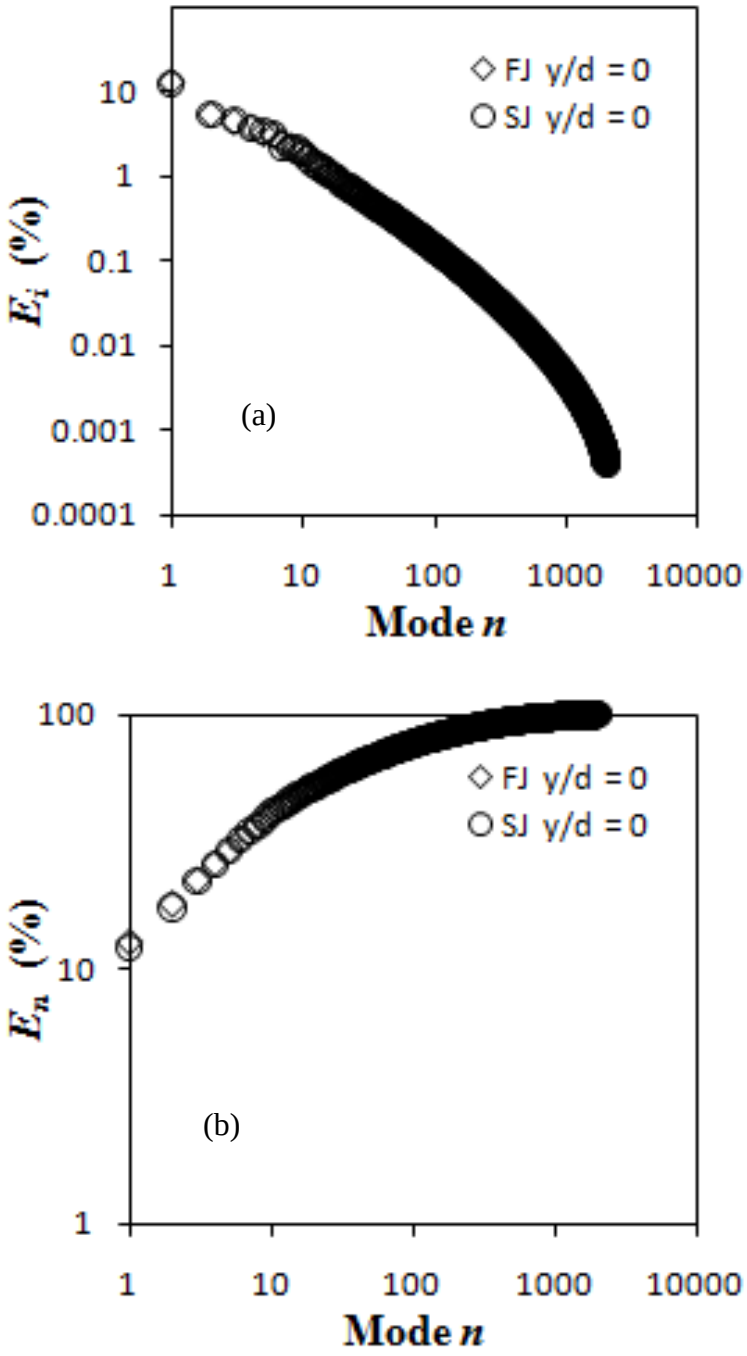

Figure 4.18 POD energy distributions in the horizontal central planes at $42 \leq x/d \leq 62$ (a) Fractional contribution of each POD mode to the total energy, *Ei*. (b) Cumulative energy distribution, *En*.

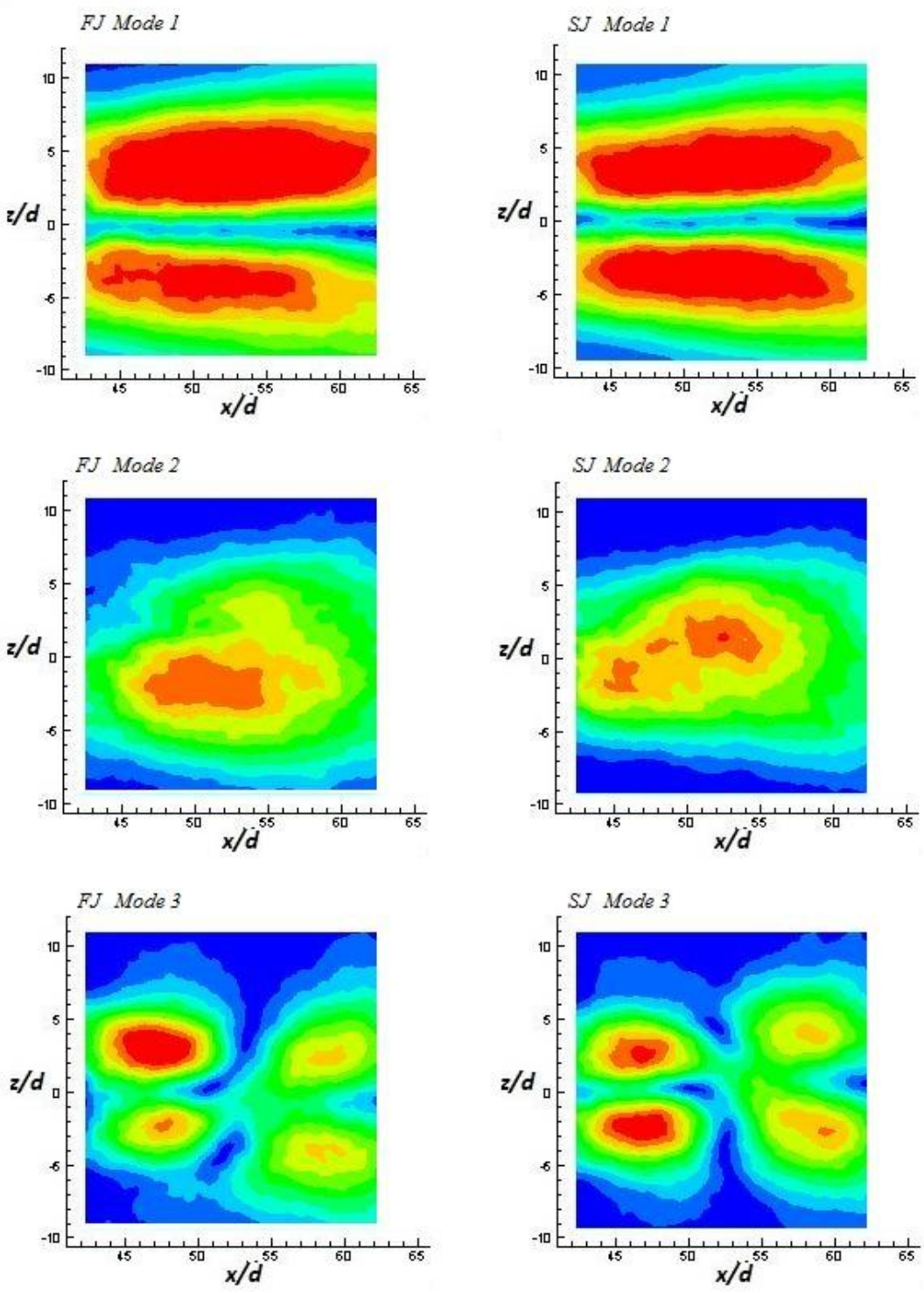
FJ Mode 1
SJ Mode 1
FJ Mode 2
SJ Mode 2
FJ Mode 3
SJ Mode 3
z/d
x/d
10
5
0
-5
-10
45
50
55
60
65

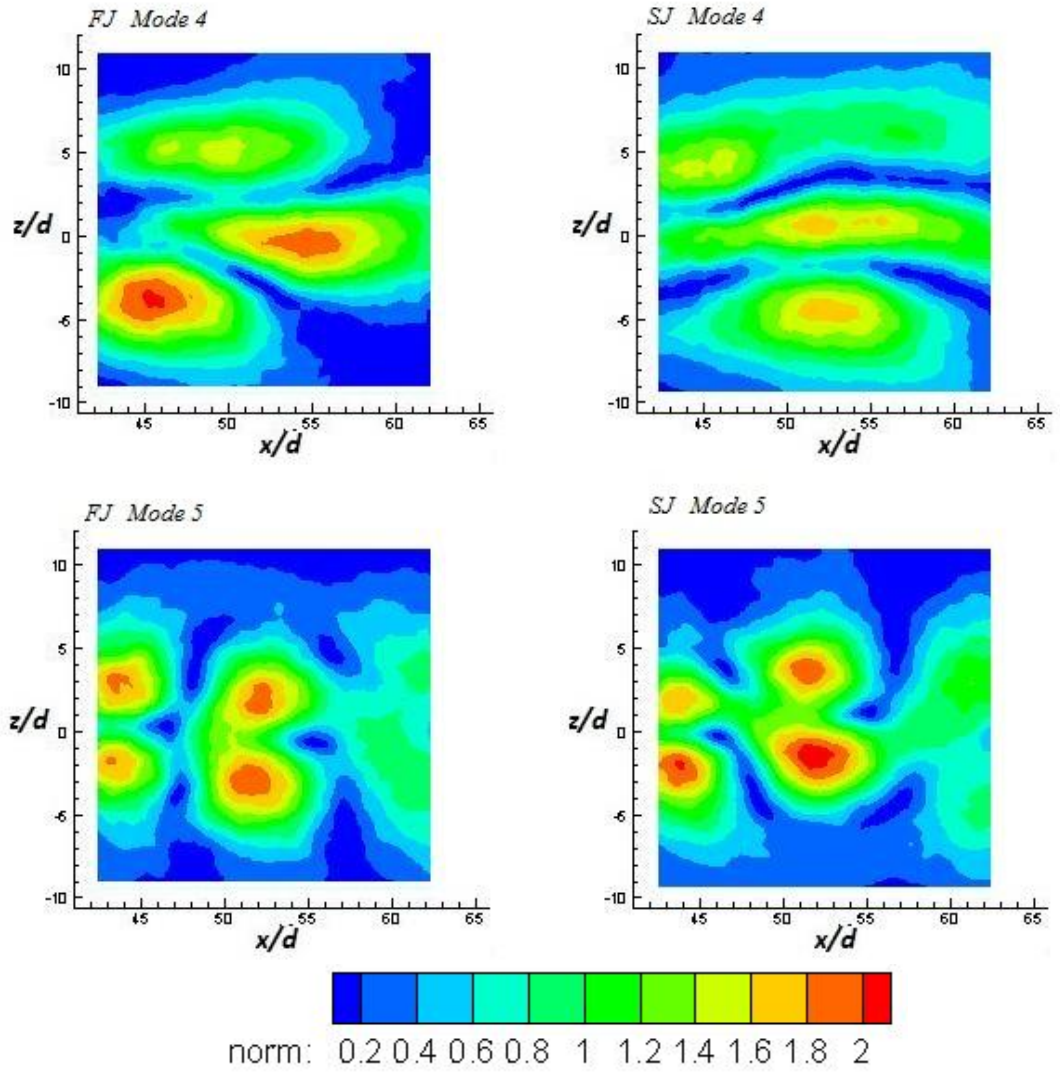

Figure 4.19 Contours of the first five POD modes in horizontal central planes for free jet (first column) and surface jet (second column).

Table 4.2 The number of POD modes used in the reconstruction to capture 50% TKE

y/d =	-4	-3	-2	-1	0	1	2	3	4
FJ	11	12	14	16	18	17	15	14	11
SJ	13	14	17	16	18	18	17	16	13

One of the advantages of the POD is the ability to obtain low- and high- pass filtered instantaneous velocity fields in order to study the physics of larger and smaller scales. Large-scale velocity fields are generated by reconstructing each individual fluctuating velocity field from the most energetic POD modes. In the present study, the number of modes employed in this reconstruction is chosen to be the minimum number required to capture 50% of the resolved TKE. The number of modes used for each FOV is listed in Table 4.3. The resulting reconstructed velocity fields represent the large scales while the difference between the original fluctuating velocity field and reconstructed velocity field represent smaller-scale field (residual velocity fields). It should be noted that the residual fields contain the remaining 50% of the TKE. As seen in the Table 4.3, the number of modes needed to capture 50% of the TKE is slightly more in the case of surface jet. It is also noticed that in the planes away from the central plane, the number of modes needed to capture 50% of the TKE is reduced for both free and surface jets.

Figures 4.20a, 4.20b and 4.20c show a typical example of an instantaneous original fluctuating velocity field, reconstructed large-scale velocity field and residual velocity field, respectively. The large-scale structure is not visible from the original instantaneous velocity field (Figure 4.20a), while it is clearly seen in the reconstructed large-scale velocity field (Figure 4.20b). The pattern of residual velocity field (Figure 4.20c) is very similar to the original velocity field with smaller velocity vectors. Although the energy contained in the individual small-scale structures is significantly less than a large-scale structure, the small-scale structures are very important due to the large magnitudes of the velocity and the large number of structures.

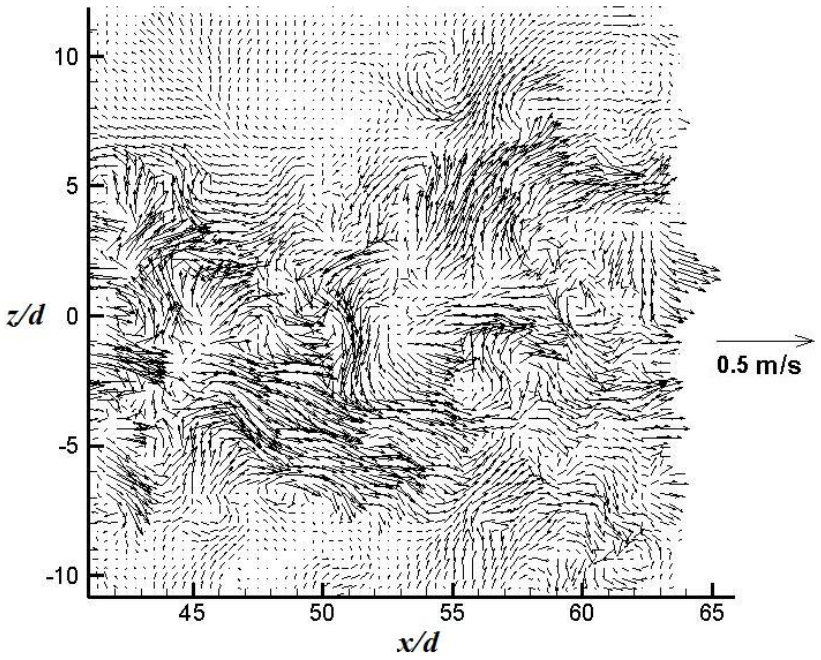

(a) Original fluctuating velocity field

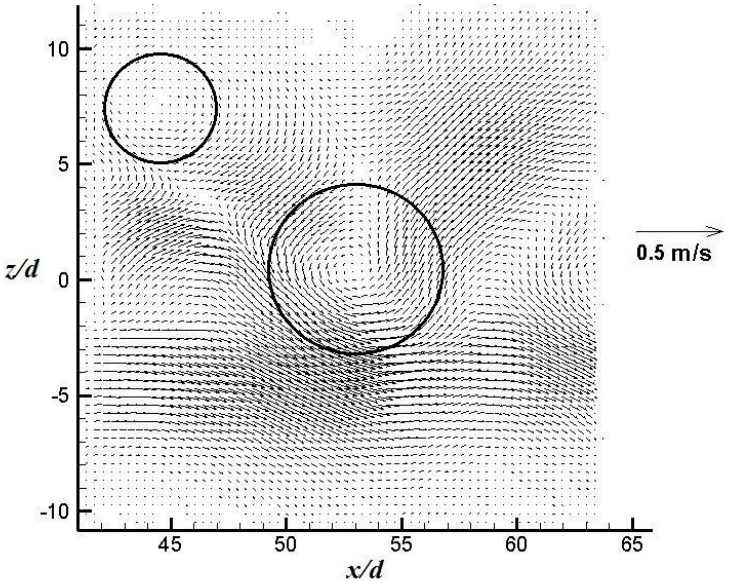

(b) POD reconstructed large-scale velocity field

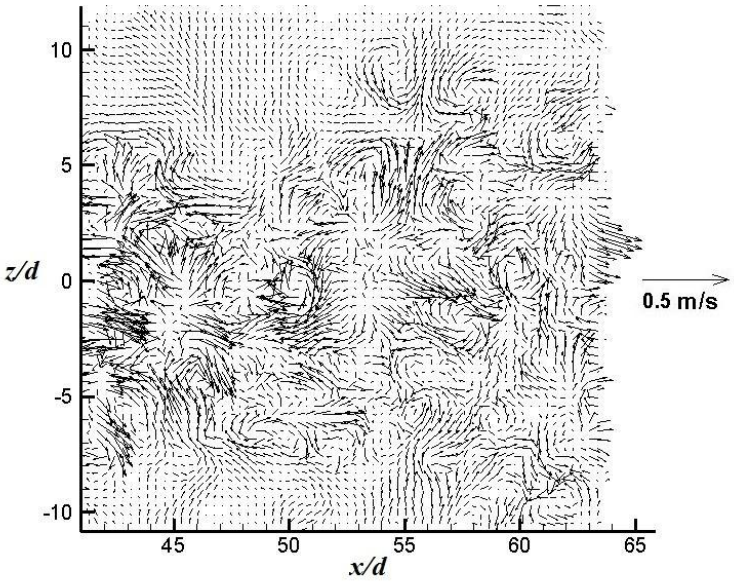

(c) Residual velocity field

Figure 4.20 Example of instantaneous velocity field, (a) original fluctuating velocity field, (b) POD reconstructed large-scale velocity field and (c) residual velocity field.

While visualization of the reconstructed large-scale and residual velocity fields provides a glimpse of the large- and small-scale features of these flows, it does not provide quantitative measures of the influence on these spatial scales. Instead, one can compute contributions of the larger and smaller scales to the turbulence intensities and shear stresses for both free and surface jets. This process generates the turbulence intensities and shear stresses attributable to the larger and smaller spatial scales, respectively, and comparison of these profiles to the total profiles provides a measure of the importance of these spatial scales to the overall turbulence intensities and shear stress in both free and surface jets.

Figure 4.21 presents contours of U_{rms} computed from the original fluctuating velocity fields as well as from the large- and small-scale velocity fields of the central plane for both free and surface jets. The contours of W_{rms} and the shear stress $\overline{uw}$ are plotted in Figure 4.22 and Figure 4.23, respectively. It is noticed that the large-scale flow contributed the majority of U_{rms} as well as shear stress $\overline{uw}$, while the small-scale flow dominates the contribution of W_{rms}. The similar trend has been found for all other measured planes (not shown here). Wu and Christensen (2010) showed a similar trend for the turbulent boundary layer. The large scales are generated in the shear layers where the lateral velocity (Figure 4.8b) is negligible. Therefore these structures are going to contribute more to the streamwise fluctuations with very small contribution to the lateral *Wrms*. The smaller structures are predominantly generated by the break up of the large scale structures and they are going to diffuse in all directions. They have smaller contribution to the U_{rms} compared to the large scale while they have significant

contribution to the W_{rms}. The major contribution to the shear stress is due to the large-scale structures as seen in Figure 4.23.

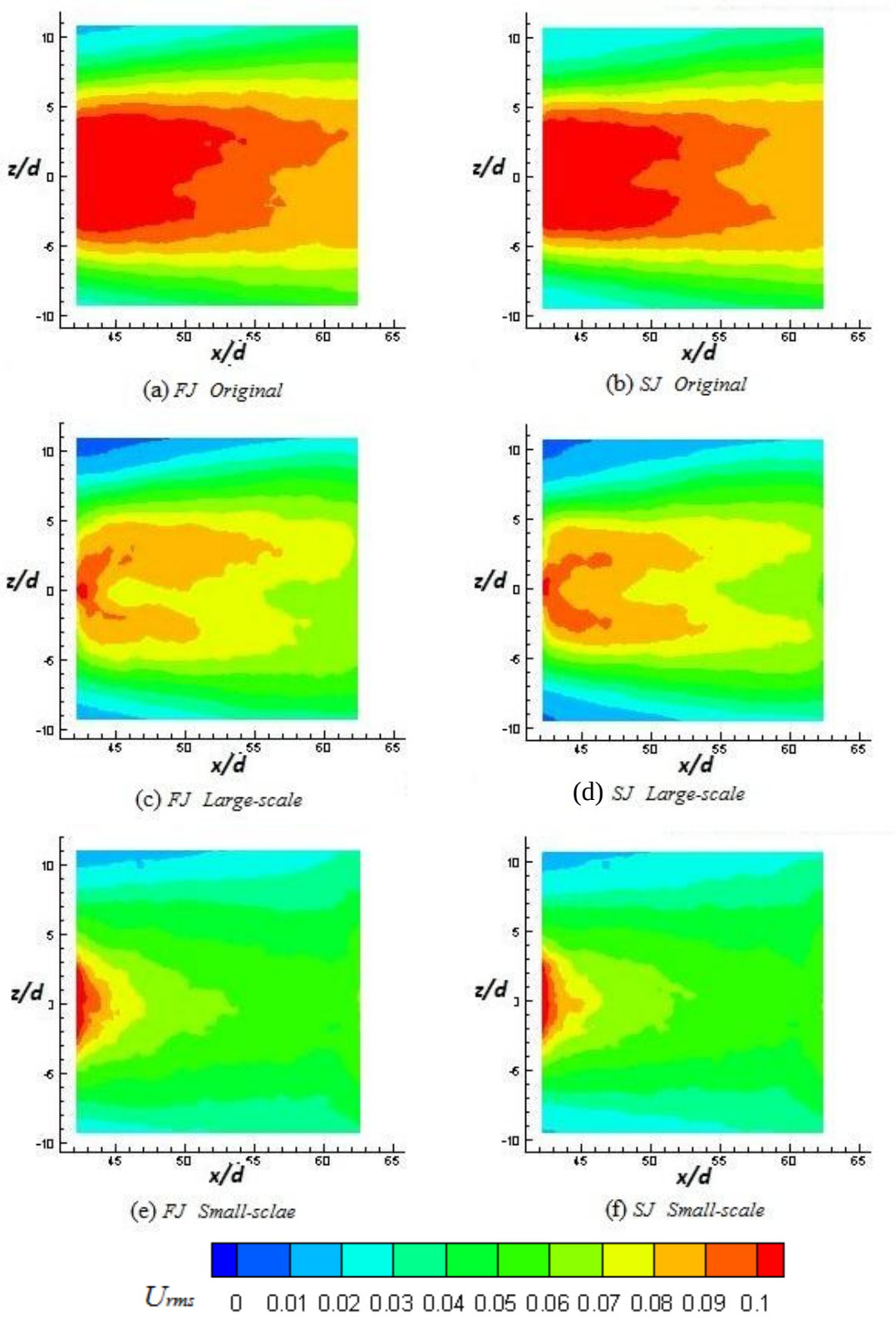

Figure 4.21 Streamwise turbulence intensity contours for free jet (first column) and surface jet (second column)

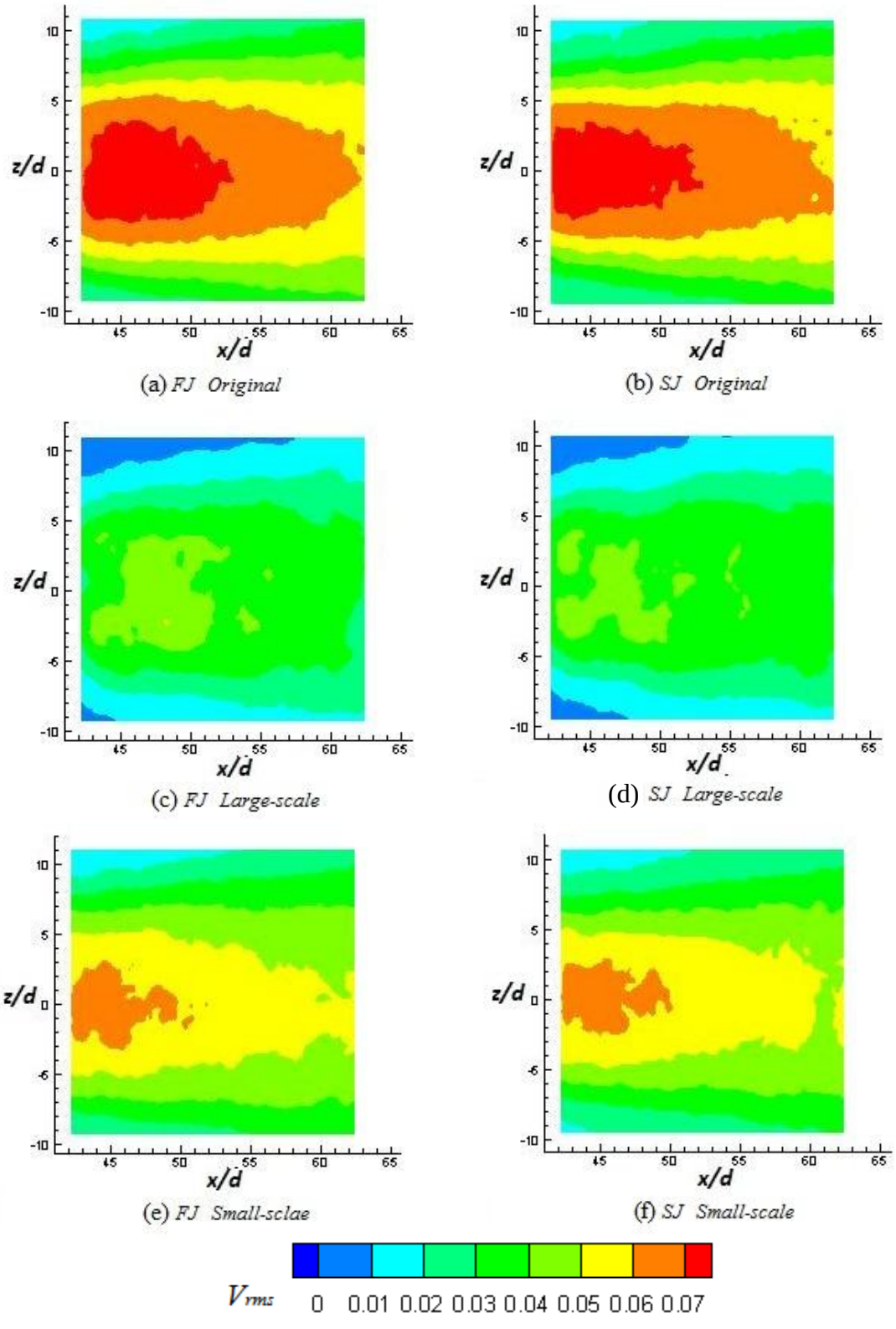

Figure 4.22 Lateral turbulence intensity contours for free jet (first column) and surface jet (second column)

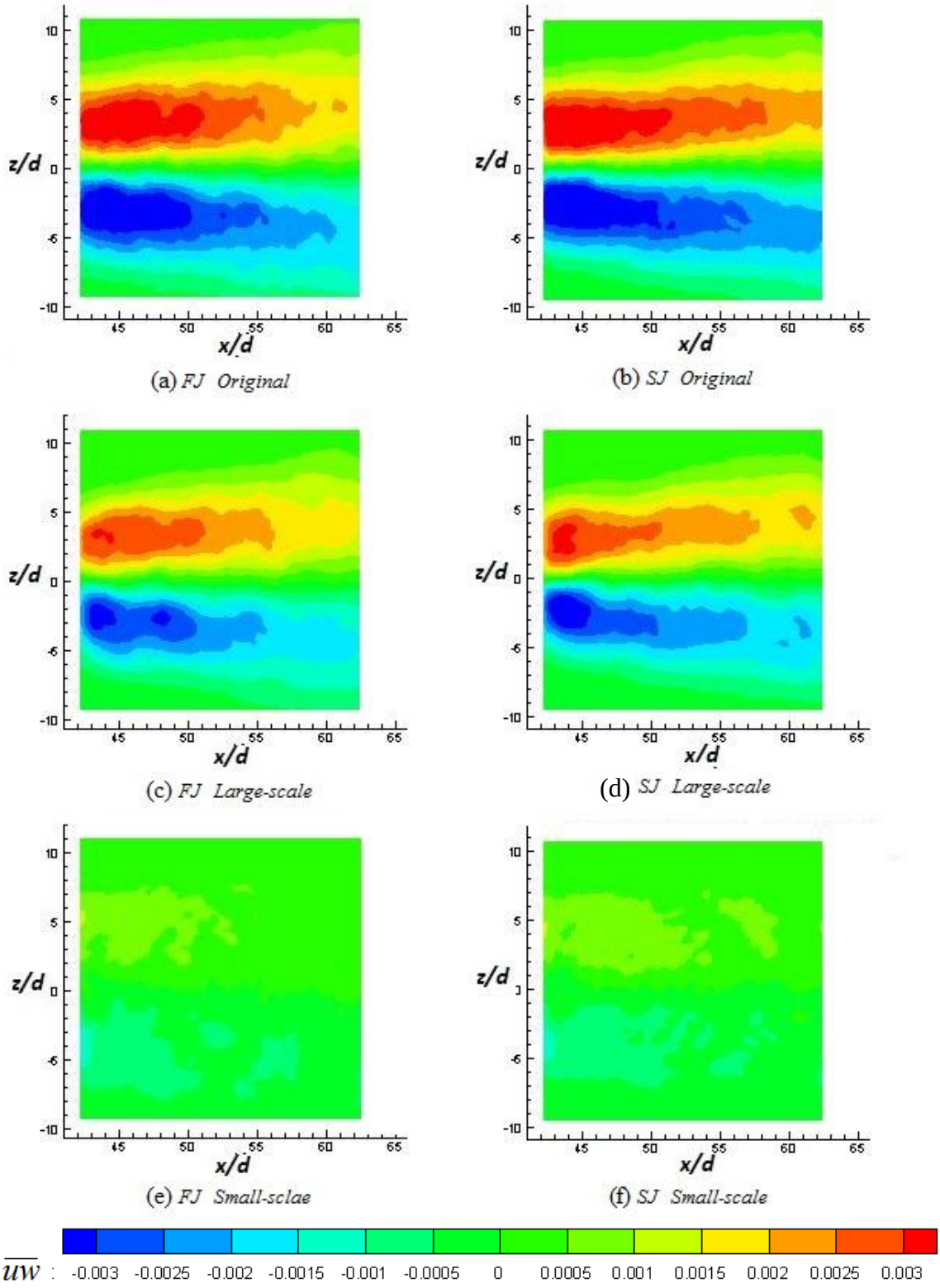

Figure 4.23 Shear stress $\overline{uw}$ contours for free jet (first column) and surface jet (second column)

CHAPTER V

CONCLUSIONS AND RECOMMENDATIONS

5.1 Conclusions

The characteristics of a round turbulent surface jet with a submergence ratio of $h/d = 5$ was investigated in this study. The Reynolds number of the flow based on the exit condition was 28,000. Velocity fields were obtained using a PIV system starting from a downstream location where the jet begins to interact with the free surface ($x/d = 30$). Measurements were obtained in the vertical central plane and several horizontal planes including the horizontal central plane for both a free jet and a surface jet. The results of the surface jet were compared with those for the free jet, and reveal that significant changes occur after the jet interacts with the free surface.

The surface jet interacts with the free surface at location about $x/d = 30$, but the effect of the free surface at this location is not significant. Beyond $x/d = 30$, the streamwise velocity profiles in the vertical central plane are shifted towards the free surface. This agrees with the results previously reported by Anthony and Willmarth (1992) and Madnia and Bernal (1994). The mean velocity profiles in the off-axis planes reveal a systematic change in the profiles in the top portion of the jet ($y/d = +1$ to $+4$). In the region near the free surface, the vertical velocity component is diminished, and the kinetic energy is redistributed, which results in enhancement of the streamwise and lateral velocities. As the downstream distance increases, the jet spreading in the region near the free surface is greater than that of the free jet. The mean lateral flow in this region tends to be outward everywhere for the surface jet, while the opposite trend has been found in the free jet.

Turbulence intensity U_{rms}, V_{rms} and W_{rms} are reduced by the effect of the free surface confinement. In the horizontal central plane, streamwise turbulence intensity appears with a typical double peak profile close to the nozzle. Those peaks are smoothened out to form a broader peak region in the central portion of the jet at the farther downstream locations. This smoothening out of the peaks occurs much faster in the surface jet compared to free jet. At sections that are away from the central plane, the U_{rms} profiles exhibit a single peak because more complete penetration by external flow has occurred in the middle region of the plane for the free jet. This characteristic is changed in the surface jet. Near the free surface, at y/d = +4, the off-axis double peaks reappear in the streamwise turbulence intensity profile because the middle portion of this plane is dominated by the mean jet flow where the turbulence intensity is lower. The V_{rms} profile shows a rapidly decreasing trend towards zero as the vertical velocity component diminishs in the region near the free surface.

The shear stress $\overline{uv}$ in the vertical central plane is decreased with increasing downstream distance and it tends to be zero in the region close to free surface. The turbulence kinetic energy production term in the vertical plane $-\overline{uv}(\partial \mathrm{U}/\,\partial \mathrm{y}\,)$ is positive and smaller in the surface jet compared to the free jet. This implies that the turbulent kinetic energy is transferred from the mean flow to the turbulence, and that transfer is significantly reduced by the free surface confinement. In identical horizontal planes, the shear stress ($\overline{uw}$) profiles are similar in both free jets and surface jets in regions where the interaction with the free surface is not significant (x/d ≈ 30). Furthermore, at x/d = 30, there is little difference between the top and bottom portions of the jet. With increasing downstream distance (45 ≤ x/d ≤ 60), near the free surface, the magnitudes of the shear

stress profiles are larger compared to that of the free jet and the bottom portion of the surface jet.

The vorticity magnitude in horizontal planes farther from the jet central plane is reduced. A higher magnitude of the vorticity in the shear layers of the surface jet are noticed compared to that of the free jet. The proper orthogonal decomposition (POD) technique was applied to the PIV data. Results show the number of modes needed to capture 50% of the turbulent kinetic energy (TKE) is slightly more in the case of surface jet. It is also noticed that the in the planes farther from the central plane, the number of modes needed to capture 50% of the TKE is reduced for both free and surface jets. In additional, the large-scale flow contributed the majority of U_{rms} as well as shear stress $\overline{uw}$, while the small-scale flow dominates towards the contribution of W_{rms}.

5.2 Recommendations for future work

The results of present study will be helpful to obtain better understanding of the free surface confinement in a round turbulent jet. Some recommendations for future study on the free surface confinement effects are summarised below:

- Further quantitative analysis of coherent structures is required to understand the behaviour of the population, size and circulation of the vortices.
- Further experimental work is needed to understand the behaviour of the surface current in the region very close to the free surface.
- The effect of submerging ratio is not investigated in the present study. A range of submergence ratio has to be studied to let further quantify the effect of the free surface.

- Stereoscopic PIV can be used to extract three-dimensional velocity fields for the study of coherent structures. This will provide more insight into the physics of the flow field.

APPENDICES

Appendix A Uncertainty analysis

The guideline of uncertainty analysis of PIV dataset was proposed by Visualization society of Japan (VSJ, 2002). Based on this procedure, a guideline of the estimation of the uncertainty of PIV dataset was put forward by the International Towing Truck Conference (ITTC, 2008). The principle of the PIV measurement on flow speed u is described as

$$u = \alpha\left(\frac{\Delta X}{\Delta t}\right) + \delta u$$

where α, ΔX, Δt are the magnification factor, displacement of the particle image, and time interval of the successive images. The magnification factor was determined by the calibration prior to the experiment. The PIV data analysis process depends on the visualization of the flow field by tracer particle and there is always a certain lag between the response of the tracer particle and the actual flow. These uncertainties consolidate into a parameter δu.

One field-of-view was selected for the uncertainty analysis is based on above procedures. The uncertainty estimates from all other field-of-views was expected of the same order of magnitude. Table A.1 shows the principal dimensions of target measurement. Calculation details are shown as following and the results are summarized in Table A.2 and Table A.3.

Error sources and propagation of errors

Image distance of the reference points: $\frac{\partial \alpha}{\partial L_r} = -\frac{l_r}{L_r^2} = -5.58 \times 10^{-5}$ [mm/pixel^2]

Physical distance from the reference point: $\frac{\partial \alpha}{\partial L_r} = \frac{1}{L_r} = 6.82 \times 10^{-4}$ [1/pixel]

Image distortion: $\frac{\partial \alpha}{\partial L_r} = -\frac{l_r}{L_r^2} = -5.58 \times 10^{-5}$ [mm/pixel^2]

Distortion in the CCD device: Presently it was assumed that there was no distortion in the CCD device and as a result, it did not contribute towards any uncertainty.

Ruler position: $\frac{\partial \alpha}{\partial l_t} = \frac{l_r}{L_r \cdot l_t} = 1.02 \times 10^{-4}$ [1/pixel]

Ruler parallelism: $\frac{\partial \alpha}{\partial \theta} = -\frac{l_r \cdot \theta}{L_r} = 0.003$ [mm/pixel]

Laser power fluctuation: $\frac{\partial X}{\partial x} = \frac{1}{\alpha} = 1.72$ [pixel/mm]

Optical distortion by CCD: It is assumed that there was no optical distortion in the CCD device.

Normal viewing angle: $\frac{\partial \alpha}{\partial \theta} = -\frac{l_r \cdot \theta}{L_r} = 0.003$ [mm/pixel]

Mismatching error: In the pixel unit analysis, mis-matching of the paired particle can take place. Large errors can be detected by comparing the vector with the surrounding vectors, and replacing them. This is the step of spurious vector detection as discussed in section 3.3. The typical uncertainty due to this error can be estimated by preparing an artificial image (Okamoto et al., 2000), and was estimated to be about 0.2 pixels.

Sub-pixel analysis: The uncertainty of the subpixel analysis depends on a number of factors, like the size of the tracer particle, noise level of the image and particle concentration. In a conservative way, the uncertainty due to this was estimated to be 0.03 pixels (Okomoto et al., 2000).

Delay generator: The delay generator controls the pulse timing and the uncertainty of that was 1×10^{-9} seconds, as found from the manual.

Pulse timing accuracy: The laser pulse has some extent of uncertainty associated with it. The typical uncertainty band, as found from the manual was 5×10^{-9} seconds.

Particle trajectory: The particle trajectory depends on the local velocity gradient and the acceleration of the flow. When the tracer particle was assumed to follow the flow faithfully, the error due to the particle trajectory was 0.01% of the total velocity. For the maximum velocity of 0.6 m/s and the uncertainty was = $0.6 \times 1000 \times 0.0001$ = 0.06 mm/s.

Three-dimensional effect: $u_{\mathrm{m}} = u + w \cdot \tan\theta = 0.62$ [mm/s]

Summary of uncertainty calculation

The individual uncertainty sources and the total uncertainty is of the instantaneous velocity is shown in Table A.3. The total uncertainty of the instantaneous velocity is estimated to be 7.02 mm/sec, or 1.17%.

Table A.1 Principal dimensions of target measurement

Target flow of measurement	
Target flow	2-D water flow
Measurement area	167.5 X 167.5 mm^2
Flow speed	0.6 m/s
Distance of reference points (l_r)	120 mm
Distance of reference image (L_r)	1467 pixels
Magnification factor (α)	0.0818 mm/pixel
Tracer particle	Spherical hollow glass particle
Average diameter (d_p)	0.012 mm
Standard deviation of diameter (s_p)	0.002 mm
Average specific gravity	1.1
Light Source	Double pulse Nd: YAG laser
Laser power	50 mJ
Thickness of laser light sheet	1.0 mm
Time interval (Δt)	0.8 ms
Camera	TSI 4MP camera
Spatial resolution	1024×1024 pixels
Sampling frequency	1.04 Hz
Gray scale resolution	8 bit
Optical system	
Distance from the target (l_t)	800 mm
Length of focus	60 mm
F number of lens	f2.8
Perspective angle (θ)	2
Pixel unit analysis	
Correlation area size	32×32 pixels
Search area size	16×16 pixels
Sub-pixel analysis	3 point Gaussian fitting

Table A.2 Uncertainty estimates from different sources for the instantaneous velocity

Parameter	Category	Error source	$u(x_i)$ (unit)	C_i (unit)	$C_i\,u(x_i)$	u_c
α (mm/pixel)	Calibration	Reference image	0.7 (pixel)	5.58×10^{-5} mm/pixel^2	3.91×10^{-5}	0.00035
		Physical distance	0.02 (mm)	6.82×10^{-4} (1/pixel)	1.36×10^{-5}	
		Image distortion by lens	4 (pixel)	5.58×10^{-5} (mm/pixel^2)	2.23×10^{-4}	
		Ruler position	0.5 (mm)	1.02×10^{-4} (1/pixel)	0.51×10^{-4}	
		Parallelism	0.087 (rad)	0.003 (mm/pixel)	2.61×10^{-4}	
ΔX (pixel)	Acquisition	Laser power fluctuation	0.0017 (mm)	1.72 (pixel/mm)	0.003	0.202
		Normal view angle	0.087 (rad)	0.003 (mm/pixel)	2.49×10^{-4}	
	Reduction	Mismatching error	0.2 (pixel)	1.0	0.2	
		Sub-pixel analysis	0.03 (pixel)	1.0	0.03	
Δt (sec)	Acquisition	Delay generator	1×10^{-9} (sec)	1.0	1×10^{-9}	5.1×10^{-9}
		Pulse time	5×10^{-9} (sec)	1.0	5×10^{-9}	
δu (mm/s)	Experiment	Particle trajectory	0.06 (mm/s)	1.0	0.06	0.622
		3-D effect	0.62 (mm/s)	1	0.62	

Table A.3 Summary of uncertainty of the instantaneous velocity

Parameter	Error source	$u(x_i)$ (unit)	C_i (unit)	$C_i\,u(x_i)$	Combined uncertainty
α	Magnification factor	0.00035 (mm/pixel)	3010 (pixels/sec)	1.05	7.02 (mm/s)
ΔX (pixel)	Image displacement	0.202 (pixel)	34.22 (mm/pixel/sec)	6.91	
Δt (sec)	Image interval	5.09×10^{-9} (sec)	0.4	2.36×10^{-9}	
δu	Experiment	0.622 (mm/s)	1	0.622	

REFERENCES

Abramovich, G.N. (1963), The theory of turbulent jets, *MIT Press.*

Anthony, D.G. and Willmarth, W.W. (1992), Turbulence measurements in a round jet beneath a free surface, *J. Fluid Mech*., v243, pp. 699-720.

Agrawal, A. and Prasad, A.K. (2002), Properties of vortices in the self-similar turbulent jet, *Exp. Fluids*, v33, n4, pp. 565-577.

Baines, W. D. and Chu, V. H. (1996), Jets and plumes, *Environmental Hydraulics*, Chapter 2, V. P. Singh and I. Hager Editors, Kluwer Academic Publishers, pp. 7-61.

Berkooz, G., Holmes, P. and Lumley, J.L. (1993), The proper orthogonal decomposition in the analysis of turbulent flows, Ann. Rev. *J. Fluid Mech*., v25, pp. 539-575.

Brown, G.L. and Roshko, A. (1974), On density effects and large structure in turbulent mixing layers, *J. Fluid Mech*., v64, part 4, pp. 775-816.

Cenedese, A., Doglia, G. and Romano, G.P. (1994), LDV and PIV velocity measurements in free jets, *Experimental Thermal and Fluid Science*, Vol. 9, pp. 125-134

Clift, R., J. R. Grace, and M. E. Weber (1978), Bubbles, drops, and particles, *Academic Press*, New York,

Dahm, W.J.A. and Dimotakis, P.E. (1990), Mixing at large Schmidt number in the self-similar far field of turbulent jets, *J. Fluid Mech*, v217, pp. 299-330.

Dimotakis, P.E., ,Miake-Lye, R.C., and Papantoniou, D.A. (1983), Structure and dynamics of round turbulent jets, *Phy. Fluids*, v26, n11, pp. 3185-3192.

Evans, J. T. (1955), Pneumatic and similar breakwaters, *Proc. R. Soc. Lond*. A 231, pp. 457-466.

Fiedler, H.E. (1987), Coherent structures in turbulent flows, *Prog. Aerospace Sci*., v25, pp. 231-269.

Graftieaux, L., Michard, M. and Grosjean, N. (2001), Combining PIV, POD and vortex identification algorithms for the study of unsteady turbulent swirling flows, Meas. Sci. Technol., v12, pp. 1422-1429.

Holmes, P., Lumley, J.L. and Berkooz, G. (1996), Turbulence, coherent structures, dynamical systems and symmetry, *Cambridge University Press*, NY, USA.

Hussain, A.K.M.F. (1983), Coherent structures - reality and myth, *Phys. Fluids*, v26, n10, pp. 2816-2850.

Hussain, A.K.M.F and Clark, A.R. (1981), On the coherent structure of the axisymmetric mixing layer: a flow visualization study, *J. Fluid Mech*., v104: pp. 263-294.

Hussain, A.K.M.F. and Zedan, M.F. (1978a), Effect of the initial condition on the axisymmetric free shear layer: Effects of the initial momentumthickness, *Phys Fluids*, v21, pp 1100-1112.

Hussain, A.K.M.F. and Zedan, M.F (1978b). Effect of the initial condition on the axisymmetric free shear layer: Effects of the initial fluctuation level, *Phys Fluids*, v**21**, pp 1475-1481.

Hussain, A. K. M. F. and Zaman, K. B. M. Q. (1981), The preferred mode of the axisymmetric jet, *J. Fluid Mech.* v110, pp. 39-71.

Hussein, H.J., Capp, S.P. and George, W.K. (1994), Velocity measurements in a high-Reynolds-number, momentum-conserving, axisymmetric, turbulent jet, *J. Fluid Mech*., v258, pp. 31-75.

ITTC (2008), Uncertainty analysis: particle image velocimetry, International Towing Tank Conference.

Kosambi, D. D. (1943), Statistics in function space, *J. Indian Math. Soc*., v7, pp. 76–88.

Launder, B.E. and Rodi, W. (1983), The turbulent wall jet measurements and modeling, *Ann. Rev. Fluid Mech*. v15, pp. 429-459.

List, E. J. (1982), Turbulent jets and plumes, *Ann. Rev. Fluid Mech*. v14, pp. 189-212.

Madnia, C.K. and Bernal, L.P. (1994), Interaction of a turbulent round jet with the free surface, *J. Fluid Mech*. v261, pp. 305-332.

Lumley, J. L. (1967), The structure of inhomogeneous turbulent flows. In *Atmospheric Turbulence and Radio Wave Propagation* (ed. A. M. Yaglom & V. I. Tatarsky), pp. 166-178. Nauka, Moscow

Okoamoto, K., Nishio, S., Saga, T., and Koboyashi, T. (2000), Standard images for particle image velocimetry, *J. Meas. Sci. Tech.*, v11, pp. 685-691.

Prasad, A. K., Adrian, R. J., Landreth, C. C., and Offutt, P. W. (1992). Effect of resolution on the speed and accuracy of particle image velocimetry interrogation, *Exp. Fluids*, v13, pp. 105–116.

Rajaratnam, N. (1976), *Turbulent Jets*, Elsevier Scientific Publishing Company, Amsterdam.

Rajaratnam, N. and Humphries, J.A. (1984), Turbulent non-buoyant surface jets, *IAHR J. Hydr. Research*, Vol. 22, No. 2, pp. 103-114

Robinson, S.K. (1991), Coherent motions in the turbulent boundary layer, *Ann. Rev. Fluid Mech*., v23, pp. 601-639.

Sankar, G., Carriveau, R. and Balachandar, R. (2005), Characteristics of confined three dimensional jets near a free surface, *17th Canadian Hydrotechnical Conference*, Edmonton

Shinneeb, A.M. (2006), Confinement effects in shallow water jets, *Ph.D. Thesis*, Dept. of Mechanical Engineering, University of Saskatchewan.

Shinneeb, A.M., Bugg, J.D. and Balachandar, R. (2004), Variable threshold outlier identification in PIV data, *Meas Sci Technol*, v15, pp. 1722-1732.

Shinneeb, A.M., Bugg, J.D. and Balachandar, R. (2008), Analysis of coherent structures in the far-field region of an axisymmetric free jet identified using particle image velocimetry and proper orthogonal decomposition, *J. Fluids Eng.*, v130, is. 1, pp. 21-29.

Sirovich, L. (1987), Turbulence and the dynamics of coherent structures. Part I: Coherent structures, *Quarterly of Applied Math*., v45, n3, pp. 561-571.

Tandalam, A., Balachandar, R. and Barron, R. (2010), Reynolds number effects on the near-exit region of turbulent jets, *J. Hydr. Engrg*. v136, is. 9, pp. 633-641.

Tso, J. and Hussain, F. (1989), Organized motions in a fully developed turbulent axisymmetric jet, *J. Fluid Mech*. v203, pp. 425.

VSJ (2002), Visualization Society of Japan, Handbook of particle image velocimetry, *Morikita publishing* (Japanese)

Weisgraber, T. and Liepmann, D. (1998), Turbulent structure during transition to self-similarity in a round jet, *Exp. Fluids*, v24, pp.210-224.

Wu, Y. and Christensen, K. T. (2010), Spatial structure of a turbulent boundary layer with irregular surface roughness. *J. Fluid Mech.*, v455**,** pp. 380-418.

Wygnanski, I. and Fiedler, H. (1969), Some measurements in the self-preserving jet, *J. Fluid Mech.*, v38, part 3, pp. 577-612.

Xu, G. and Antonia, R.A. (2002), Effect of different initial conditions on a turbulent round free jet, *Exp. Fluids*, v33, n5, pp. 677-683.

VITA AUCTORIS

Jiahao Tian was born in QianJiang, CHINA in 1981. He earned his first Bachelor degree in the discipline of Computer Science from Wuhan University of Technology, Wuhan, CHINA in 2003. He enrolled in the department of Mechanical Engineering in University of Windsor in 2005 and graduated in 2008 with a Bachelor of Applied Science. He continued his study in University of Windsor leading to the degree of Master of Applied Science in Mechanical Engineering.